

Development of multi-point fiber Bragg grating sensors combined with incoherent FMCW optical ranging system

メタデータ	言語: eng 出版者: 公開日: 2020-10-30 キーワード (Ja): キーワード (En): 作成者: メールアドレス: 所属:
URL	http://hdl.handle.net/2297/00059756

This work is licensed under a Creative Commons Attribution-NonCommercial-ShareAlike 3.0 International License.



Dissertation

*DEVELOPMENT OF MULTI-POINT FIBER BRAGG GRATING
SENSORS COMBINED WITH INCOHERENT FMCW OPTICAL
RANGING SYSTEM*

Graduate School of
Natural Science & Technology
Kanazawa University

Optical and Electronic Sensing Laboratory
Division of Electrical Engineering and Computer Science

Student ID Number : 1724042004
Name : Dwi Hanto
Chief Supervisor : Prof. Koichi Iiyama
Date of Submission : January 2020

Table of Contents

ACKNOWLEDGMENT	5
ABSTRACT	7
LIST OF FIGURE	9
LIST OF TABLE	12
ABBREVIATIONS	13
CHAPTER 1: INTRODUCTION.....	15
1.1 Overview	15
1.2 State of the art	16
1.3 Objective	18
1.4 Outline.....	19
CHAPTER 2: FBG SENSOR.....	21
2.1 Theory of FBG.....	21
2.2 FBG Fabrication Techniques.....	23
2.3 Sensing Principle	24
2.4 Measurement method	26
2.5 Peak of Bragg wavelength tracking.....	32
2.6 FBG measurement	35
2.7 Summary	37
CHAPTER 3: VCSEL	38
3.1 Structure of VCSEL.....	38
3.2 Theory of VCSEL.....	40
3.3 Tunable wavelength of VCSEL.....	43
3.4 Modulation of VCSEL	45

3.5	Measurement of VCSEL wavelength	47
3.6	Summary	49
CHAPTER 4: FMCW		51
4.1	Basic and principle of FMCW	51
4.2	Analysis of FMCW Signal	52
4.3	Incoherent FMCW	55
4.4	Fast Fourier transform (FFT) processing.....	57
4.5	Summary	59
CHAPTER 5: DEVELOPMENT OF FBG INTERROGATOR SYSTEM... 60		
5.1	Set up of FBG interrogator	60
5.2	Development a software.....	61
5.3	Frequency response.....	64
5.4	Summary	65
CHAPTER 6: LONG-RANGE AND SPATIAL RESOLUTION MEASUREMENT..... 66		
6.1	Measurement of long-range optical fiber.....	66
6.2	Spatial resolution measurement	68
6.3	Identification of sensor location.....	70
6.4	Summary	71
CHAPTER 7: TEMPERATURE MEASUREMENT..... 72		
7.1	Temperature FBG identification by scanning wavelength.....	72
7.2	Spectrum Profile of FBG when temperature change.....	75
7.3	Transfer function of FBG temperature sensor.....	75
7.4	Long term stability testing.....	76
7.5	Summary	77

CHAPTER 8: STRAIN MEASUREMENT.....	79
8.1 Principle of strain measurement based on a cantilever beam.....	79
8.2 Strain FBG identification by scanning wavelength	80
8.3 Spectrum profile when FBG strain change	82
8.4 Transfer function of strain FBG sensor	83
8.5 Cross-sensitivity and decreased magnitude issue.....	83
8.6 Summary	84
CHAPTER 9: CONCLUSION.....	85
9.1 Summary	85
9.2 Future Works	85
REFERENCE	87
PUBLICATION	95

Acknowledgment

In the name of Alloh, the Gracious, the Merciful. All praise to be Alloh almighty for giving me strengths and ability to complete my dissertation and achievement in the Ph.D. study at Kanazawa University.

I would like to express my special thanks of gratitude to my supervisor, Prof. Koichi Iiyama, who gave me full support, guidance, and valuable advice during the study and also when conducting research at Kanazawa University. It was to be an honor to join an excellent laboratory and to have an opportunity doing interesting topic research over three years and three months. I am also really grateful to my advisor, Assoc. Prof. Takeo Maruyama, who kindly valuable advice not only for research but also for living in Japan. I also would like to thank members of my dissertation committee: Assoc. Prof. Toshiyuki Ueno, Assoc. Prof. Yuji Kuwamura, and Assoc. Prof. Satoshi Sunada, for their insightful comments, to improve my research. Also, I thank all members of Optical and Electronic Sensing Laboratory (Oeslab): Dr. Zul Athfy, Rini san, Sartika san, Chen san, Noguchi San, Ikeda san, Nakamura san, Ooka san, Kitamura san, Sato san, Nakamoto san, Yamaguchi san, Washizuka san, Misaki san, Masaki san, Iseki san, and Minamizawa san.

I would like to thank deeply to all my family, especially my parents Mrs. Suliyati and Mr. Marimin, my siblings Eko and Triwi, my parents in law Mrs. Yatinah and Mr. Sastro, for their endless support and du'aa. Most special to my little family, my sweetheart Yuliati and my lovely kids: Hassan Syahim, Alyssa Syahima, and Essam Hiroshi Syahim for your unconditional love every time. You always beside me to cross a new journey in Japan, no matter winter or summer. We all together, have learned and experienced here. Hopefully, we will be a strong family.

I am very grateful to Ministry for Research and Technology, the Republic of Indonesia, through the Program for Research and Innovation in Science and Technology (RISET-Pro) Scholarship, which supported whole my study at Kanazawa University. Especially thanks to Dr. Acep Purqon, who has introduced and brought me an excellent campus, Kanazawa University.

I want to thank all staff of Kanazawa University, Japanese Class teachers, GS II Program team, International Student Center, and Japanese Class teachers at Morinosato Elementary School and Izumi Elementary School for their kind to help us during stayed in Japan.

Finally, I also very grateful to my institution, the Indonesian Institute of Sciences (LIPI), especially for my colleagues in Optoelectronic's research group. We hope we can contribute significantly to increase our country through research in Optoelectronics. Further, I thank my colleagues and friends: Risproers at Kanazawa University, Indonesian Student Association in Japan (PPI) Hokuriku chapter and Ishikawa commissariat for their friendship, for making me enjoy discovering all the best experience in Japan.

Kanazawa, February 5th, 2020

Dwi Hanto

Abstract

My dissertation presents and discusses a method to develop an FBG interrogator for long-range structural health monitoring systems (SHMS) applications. More than many years, multipoint sensors become an interesting system in research and practice as well, especially for very large and very long SHMS. Recently, multipoint sensors involving fiber Bragg gratings (FBGs) have been widely used in the SHMS due to have some advantages than traditional sensors.

In our dissertation, a three-points FBG sensor, which has nearly similar Bragg wavelength and reflectivity, is successfully analyzed by a combination of incoherent frequency modulated continuous wave (I-FMCW) optical ranging system and a vertical-cavity surface-emitting laser (VCSEL) as a wavelength-tunable laser source. Our system can provide not only reading out the temperature and strain by using FBG sensors, but also identifying the location of the installed FBGs. The I-FMCW optical ranging system can be conducted by intensity modulation of a low-cost commercial VCSEL by linearly sinusoidal waveform from a signal generator. In order to explore the Bragg wavelength, the wavelength of the VCSEL can also be swept by the injection current change in step. The detected signals from the FBGs, which captured by a photodiode, and the reference signal from the signal generator, are electrically mixed by a double-balanced mixer (DBM) to define the beat frequency. All system is controlled by a program developed by LabVIEW from National Instruments (NI).

We demonstrate our proposed system to measure long-range, temperature, and strain measurements. The measurement result shows that our system can clearly distinguish all FBGs installed in a totally 6.6 km-long optical fiber with 1.5 m spatial resolution. For temperature measurement, we use a thermoelectric controller (TEC) to control the ambient temperature of FBG1 in the range of 25°C ~ 45°C, and contrary, the others are kept at room temperature. The Bragg wavelength shifts of the FBGs according to temperature changes are successfully measured. We also test the stability of measurement in temperature in our laboratory for 23 hours. The results show that error measurement less than 2°C for

all FBGs. As well as measuring temperature, we also conduct strain measuring. FBG3 is strained in the range of $369 \mu\epsilon \sim 2137 \mu\epsilon$ by using cantilever beam method, and contrary the others are unstrained. The results show that the Bragg wavelength shift of the FBGs according to strain changes are also successfully measured. Temperature and strain sensitivity from measurement results by using our system is almost same if compared to other methods and theory.

Our system only experimentally tested in the temperature range $25^{\circ}\text{C} \sim 45^{\circ}\text{C}$ and in the strain range of $369 \mu\epsilon \sim 2137 \mu\epsilon$. Nevertheless, there will be opportunities to span more large temperature and strain range by increasing injection current to sweep more wavelength change. Even though our system tested only three FBGs in the experiment, the system can be scaled up to more FBGs and extended scale areas. Furthermore, because we employed a low-cost available VCSEL, our proposed system offers a low-cost and straightforward FBG interrogator for a long-range SHMS.

Key words: VCSEL, FMCW, FBG, SHMS.

List of figure

Figure 1. Model of the FBG structure [31].	22
Figure 2. Bragg diffraction on atom lattice [32].	22
Figure 3. Reflectivity spectrum of FBG for two different values of kL (2 and 8)[35].	23
Figure 4. FBG fabrication by using (a) phase mask (b) point to point with fs-IR [31].	24
Figure 5. Shift of Bragg wavelength in FBG [35].	26
Figure 6. Principle of Bragg wavelength measurement [41].	27
Figure 7. Bragg wavelength measurement by using OSA [44].	27
Figure 8. Bragg wavelength measurement by using a tunable laser [44].	28
Figure 9. Bragg wavelength measurement by using CCD-spectrum [45].	28
Figure 10. Bragg wavelength measurement by using TDM [46].	29
Figure 11. Bragg wavelength measurement by using WDM [47].	29
Figure 12. Bragg wavelength measurement by using TPA [48].	30
Figure 13. Bragg wavelength measurement by using OTDR [49].	31
Figure 14. Bragg wavelength measurement by using OFDR [51].	31
Figure 15. Peak tracking by X-dB bandwidth method [53].	33
Figure 16. Peak tracking by centroid method.	34
Figure 17. Peak tracking by 2 nd order polynomial [53].	35
Figure 18. Peak tracking by Gaussian polynomial fit [53].	35
Figure 19. Temperature sensing measurement by using FBG sensor.	36
Figure 20. Strain sensing measurement by using FBG sensor.	36
Figure 21. Structure of VCSEL [21].	38
Figure 22. DBRs structures in VCSEL [23].	39
Figure 23. Light-current-voltage curve of VCSEL [61].	41
Figure 24. Injected current scheme and output response of VCSEL [21].	44
Figure 25. Wavelength change as a result of injection current on VCSEL[21].	44
Figure 26. Bias T circuit for direct modulating a VCSEL.	46
Figure 27. External modulation on VCSEL by using modulator [65].	46

Figure 28. Frequency modulation response of VCSEL for different bias current[61].	47
Figure 29. Set up the measurement of a shift of VCSEL wavelength by using injection current.	48
Figure 30. Influence of VCSEL case temperature change in wavelength shift. ...	49
Figure 31. Correlation between injection current on VCSEL with wavelength, with the temperature of VCSEL case 20°C.	49
Figure 32. Sawtooth wave modulation FMCW [64].	53
Figure 33. Triangular wave modulation FMCW analysis [64].	53
Figure 34. Triangular wave modulation FMCW [64].	54
Figure 35. Configuration of the I-FMCW optical ranging system.	55
Figure 36. I-FMCW signal analysis.	56
Figure 37. FFT signal with main lobe and sidelobe [72].	58
Figure 38. Configuration of the proposed system for FBG interrogator.	61
Figure 39. Flowchart of LabVIEW program for the proposed system.	63
Figure 40. GUI of the FBG interrogator based on I-FMCW.	64
Figure 41. Frequency response of the proposed system.	64
Figure 42. Group delay of the proposed system.	65
Figure 43. Illustration of long-range measurement for length of the optical fiber; (a). 1000 m and (b) 6640 m.	66
Figure 44. Measured beat spectrum of Fresnel reflection of an optical fiber with length of (a) 1000 m and (b) 6640 m.	67
Figure 45. Illustration of long-range measurement with three FBGs.	68
Figure 46. Measured beat spectrum for different FO3 length, (a) 40 m, (b) 5 m, (c) 3 m at the same temperature, and unstrained.	69
Figure 47. The spatial resolution of reflection of FBG.	70
Figure 48. Illustration of temperature measurement by using the proposed system.	72
Figure 49. Measured beat spectrum for wavelength of (a) 1560.740 nm and (b) 1560.955 nm when the temperature of the FBG1 is 40°C, and the temperature of the FBG2 and FBG3 are room temperature (approximately 23°C).	73

Figure 50. Measured beat spectrum for wavelength of 1560.774 nm when temperature of all FBGS at room temperature.....	74
Figure 51. Spectrum of (a) FBG1, (b) FBG2, and (c) FBG3 when the temperature of FBG1 is changed.....	74
Figure 52. Transfer function of temperature FBG sensor.....	75
Figure 53. Stability and reliability testing of the proposed system for 23 hours. .	77
Figure 54. Strain measurement by using the cantilever beam method.	80
Figure 55. Illustration of measurement strain measurement using the proposed system.....	81
Figure 56. Measured beat spectrum for wavelength of (a) 1560.703 nm, (b) 1560.187 nm. FBG1 and FBG2 are unstrained, and FBG3 is strained at 722 $\mu\epsilon$.	81
Figure 57. Spectrum of (a) FBG1, (b) FBG2, and (c) FBG3 when FBG3 is strained and FBG1 and FBG2 are unstrained.	82
Figure 58. Transfer function of strain FBG sensor.	83

List of table

Table 1. Specification of FBG1, FBG2, and FBG3.	61
Table 2. FBGs location identification.	70

Abbreviations

FBG	: fiber Bragg grating
FMCW	: frequency modulated continuous wave
I-FMCW	: incoherent frequency modulated continuous wave
C-FMCW	: coherent frequency modulated continuous wave
SHMS	: structural health monitoring systems
VCSEL	: vertical-cavity surface-emitting laser
DBM	: double-balanced mixer
NI	: National Instruments
TEC	: thermo-electric controller
ETDR	: electrical time-domain reflectometers
MEMS	: microelectromechanical sensor
OSA	: optical spectrum analyzer
CCD	: charge-coupled device
LD	: laser diode
FDML	: Fourier-domain mode-locking
WDM	: wavelength-division multiplexing
TDM	: time-division multiplexing
SNR	: signal and noise ratio
OFDR	: optical frequency domain reflectometry
C-OFDR	: coherent optical frequency domain reflectometry
I-OFDR	: incoherent frequency-domain reflectometry
VNA	: vector network analyzer
FWHM	: full width at half maximum
UV	: ultraviolet
fs-IR	: femtosecond pulse infrared
ASE	: amplified spontaneous emission
TPA	: two-photon absorption
OTDR	: optical time-domain reflectometry
DBR	: distributed Bragg reflectors
MQW	: multiple quantum wells

mA	: mili Ampere
InP-InGaAsP	: Indium Phosphide-Indium Gallium Arsenide Phosphide
FSR	: free spectral range
RIN	: relative intensity noise
EA	: electro-absorption
nm	: nanometer
OPD	: optical path different
Radar	: radio detection and ranging
LPF	: low pass filter
Hz	: Hertz
kHz	: kilo Hertz
MHz	: mega Hertz
FFT	: fast Fourier transform
RF	: radio frequency
DAQ	: data acquisition
TTL	: transistor-transistor logic
PC	: personal computer
GPIO	: general-purpose interface bus
GUI	: graphical user interface
RMS	: root mean square
PD	: photodetector
km	: kilo meter
dB	: decibel
A.u	: arb.unit
RMSE	: root mean square error

CHAPTER 1: INTRODUCTION

1.1 Overview

In recent years, technology is rapidly growing up in the world. Thus, many countries now have a lot of huge of civil infrastructures like skyscrapers, water DAMs, tunnels, long bridges, and highways represent an enormous financial investment. These buildings can be seen not only in developed countries but also in developing countries. Unfortunately, several accidents caused structures collapses that have been killed many people [1]. Therefore, engineers, researchers, and also stakeholders have been struggling to overcome this problem. Consequently, there is an urgent need to develop a system that early detection of the structural health problems in order to prevent more serious damage.

On the other hand, many advances in sensing, computing, and communications create a new technology to solve the health of structures detection, which is a structural health monitoring system (SHMS) [2]. SHMS is defined as a process of detecting structural conditions due to damage or deterioration by comparing structural responses obtained by various physical parameters using many kinds of sensors, both temporally and spatially. The process in SHMS covers sensors installation, comparative feature extraction, normalization, and estimation for diagnosis of structural health conditions [3]. By using this system, structures continuously and automatically detect the damage, characterize it (recognize, localize, quantify, or rate) and report it [4]. The conditions of structural health are influenced by numerous events such as loads, earthquakes, fires, explosions, collisions, and others. The influences of individual events come from strains, cracks, and temperature gradients [5].

To detect some physical parameters in structures, SHMS usually employs many kinds of sensors such as a piezoelectric sensor, strain gauge, electrical time-domain reflectometers (ETDR), a microelectromechanical sensor (MEMS), an eddy current sensor, and fiber optic sensor. The sensor mentioned at last, fiber optic sensor, has more advantages than other sensors such as it is very compact and easily embedded into structures. Besides, fiber optic sensors also offer the

capability to perform integrated, distributed measurements, and immune to electromagnetic interference; therefore, it suitable for SHMS [4], [6].

A fiber optic sensor widely used in SHMS is fiber Bragg grating (FBG). Due to FBG is leading on application-wide multiplexing of measurement points, FBG is called the king of the quasi-distributed sensors [2]. Several FBGs can be clearly resolved by using the same fiber line by multiplexing many FBGs in the wavelength domain [4]. Since FBG has a unique core whose periodic refractive index variation, a light whose wavelength satisfied the Bragg condition can measure strain and temperature [7]–[9]; those are critical parameters in SHMS.

Because the FBG based measurement system has distinctive advantages when applied in SHMS, some researchers have been making an effort to develop FBG interrogator for several years. The main issue in the FBG interrogator for SHMS applications are long-range remote sensing and spatial resolution capability. Another interesting issue, over the past decade in industrial sectors, has also been paid in attention to reduce cost and made more competitive [1]; consequently, there is also challenging in low-cost systems for FBG interrogator. Therefore, our dissertation proposes to develop an FBG interrogator not only for long-range and multi-point sensing but also offers low-cost systems.

1.2 State of the art

Over two decades, a large variety of systems for the FBG interrogator has been developed. Generally, the simplest way to interrogate FBG is by using an optical spectrum analyzer (OSA). Given that OSA has limited scanning and high-cost in the operational system, a charge-coupled device (CCD) spectrometer and using tunable Fabry-Perot filters succeed in replacing an OSA. Those methods enable to realize wavelength speed scanning up to 20 kHz [10], [11]. However, it may be rather difficult to be applied in long-range measurement because these systems need high power for the broad-spectrum light source, which is launched into FBG. For this reason, not only from the university and research center but also from the industry have proposed other methods to interrogate FBG, which are compact, low-cost, and effective in real time.

Among the FBG interrogate methods, the wavelength-swept laser is now widely used due to high intensity, narrow lasing, and wide wavelength tuning range [12]. Many kinds of wavelength-swept lasers, either laser diode (LD)-based or fiber laser-based, have been developed by using external cavity tunable LD, piezo transducer-based tunable Fabry-Perot filter, polygonal mirror scanner, and Fourier-domain mode-locking (FDML). Sweep rate can be achieved fast and widely [13], [14], but those techniques require a high cost for providing some optical or mechanical components. On the other hand, a vertical-cavity surface-emitting laser (VCSEL) has been demonstrated as a low-cost wavelength-swept by simply changing the injection current or temperature [15]–[18]. VCSEL has demonstrated remarkably good stability and reproducibility of the output frequency [19], [20] and make it promising for low-cost application involving wavelength-swept lasers such as tomography [21], object profiling [15], [22], and high-speed communication [23].

Multiplexing sensor is also one of an issue in SHMS, especially for large structures monitoring in order to know a precise location where damage is. If FBGs with different Bragg wavelength is installed for multi-point sensing, the locations can be recognized from it's Bragg wavelength. In this case, wavelength-division multiplexing (WDM) and time-division multiplexing (TDM) are introduced for Bragg wavelength demodulation. However, allowable Bragg wavelength shift is limited by the bandwidth of broadband light source, a width of the sensor window, and spatial resolution between the individual sensor [24], [25].

The large multiplexing and lower crosstalk of the FBGs sensors through both simulation and experiment could be carried out by optical reflectometry based measurement either time domain or frequency domain [26]. Time-domain reflectometry uses optical pulses launched into an optical fiber and processes backscattered signals. In order to increase the spatial resolution, the pulse width has to be reduced. However, this method requires ultrafast light modulation and detection, which is very expensive. On the other hand, since frequency-domain reflectometry measures interference of Rayleigh signal from reference and reflected signal, the spatial resolution is governed by the frequency range [27].

Besides, frequency domain reflectometry also offers high signal and noise ratio (SNR) as well as better spatial resolution than time-domain reflectometry.

Frequency-domain reflectometry can be divided into two categories; a coherent optical frequency domain reflectometry (C-OFDR) and incoherent frequency-domain reflectometry (I-OFDR). For long-range measurement applications, I-OFDR has promising opportunities instead of C-OFDR because of I-OFDR is the non-interferometric, which no requires a narrow linewidth laser and ultra-linearly swept optical source [28], [29]. By using I-OFDR, Werzinger et al. reported that 20 FBGs could be successfully interrogated by vector network analyzer (VNA). The location of FBGs is calculated by the inverse Fourier transform of the frequency response. Hence VNA is quite costly, incoherent frequency modulated continuous wave (I-FMCW), a sub-group of the I-OFDR, offers much cheaper because of this system combine reference and reflected signal in the electrical domain by using electrical mixing component [30].

1.3 Objective

To date, long-range and low-cost FBG interrogator becomes an exciting research topic, especially for SHMS applications. In this research, we propose a combination of wavelength-swept by using VCSEL and I-FMCW optical ranging to develop a new system of FBG interrogator. A wavelength-swept tunable laser can be achieved by injection current on VCSEL in order to explore the spectrum of FBGs. Compared to the other technique, it needs only a low-cost component. Then, I-FMCW is also employed in our research for the purpose of multiplexing and localizing of FBGs.

To realize this method, we set up a system consist of an I-FMCW ranging system and VCSEL as a light source. We make a program by using National Instrument (NI) LabVIEW to control our system. In order to know the performance of FBG Interrogator, which is developed by using our method, we observe as follows:

1. Long-range and spatial resolution capability
2. Temperature measurement capability
3. Strain measurement capability.

1.4 Outline

This dissertation thesis presents a proposed method to interrogate multipoint FBG sensors for long-range SHMS. This dissertation has been organized as the following chapter:

Chapter 1: We introduce the SHMS and the reason why the FBG sensor is one of a candidate to be applied in SHMS. Then, we briefly explain the state of the art from some methods of FBG interrogation for the purpose of multipoint sensor and long-range measurement. Therefore, we decided to use a combination of VCSEL and incoherent FMCW for multipoint and long-range FBG sensors measurement.

Chapter 2: We provide a theory of FBG, starting from the definition of Bragg wavelength and the principle of FBG on strain and temperature sensing. We also introduce some methods to measure Bragg wavelength and algorithm to define the peak of Bragg wavelength. In the last section, we present a result measurement of the FBG sensor for temperature and strain sensing by using a proven method, which is a broadband light source and OSA.

Chapter 3: We introduce a theory of VCSEL, including from structures, principles of the wavelength-tunable method, and how to modulate the VCSEL. In the last section of this chapter, we measure the wavelength-tunable of VCSEL by injection current change.

Chapter 4: We describe a principle ranging measurement by using FMCW. We also introduce types and signal analysis of FMCW with different types of modulation signals. In the last section, we also briefly introduce one type of FMCW ranging system, which is incoherent FMCW.

Chapter 5: We present how to set up the FBG interrogator based on I-FMCW and VCSEL. In this chapter, we also describe a development program by using LabVIEW and show the measurement examples. In the last section, before we applied our system to measure the FBG sensor, we check the frequency response of our system.

Chapter 6: We show and discuss a measurement result of long-range and spatial resolution. We make variation a length of optical fiber that connects to the FBG sensor to confirm long-range and spatial resolution capability. In the initial testing, we check Fresnel reflection of optical fiber without FBG sensor, then continue to

install three FBG sensors into a configuration with different lengths of optical fibers.

Chapter 7: In this chapter, we present and discuss a measurement result of our system when it is applied to measure temperature. We apply temperature variation on FBG1 by using TEC, whereas other FBG are kept at room temperature. We observe spectrum profile each FBGs, and then we examine the correlation between temperature and Bragg wavelength. After that, the result from our system compares to the theory and standard method by using OSA and broadband light sources. Additionally, we also test stability for 23 hours.

Chapter 8: Before we show and discuss a measurement result, we introduce a method of strain measurement based on a cantilever beam. Like temperature measurement, we also apply strain variation on FBG3, and contrary other FBGs are kept unstrained conditions. We then observe the spectrum profile and also present the correlation between strain and Bragg wavelength. The experiment result is also compared to other methods as presented in the last section on Chapter 2.

Chapter 9: in the last chapter, we will discuss and summarize the results which have been presented in Chapter 6, 7, and 8. We also propose recommendations for future research.

Chapter 2: FBG Sensor

2.1 Theory of FBG

Fiber Bragg grating (FBG) is an optical filtering device that reflects lights of specific wavelengths and is present within the core of an optical fiber waveguide, as shown in figure 1. A reflected wavelength depends on the spacing of a periodic refractive index in the fiber core [31]. The term of fiber Bragg grating came from the Bragg law of X-ray diffraction, which is established by Sir William Lawrence Bragg. The figure 2 shows the lattice structure of a crystal reflects that incident radiation. In this case, a crystalline solid with lattice plans separated by distance (d), waves are scattered and interfered constructively when path length of each wave is equal to an integer multiple of the wavelength as described in the equation 1.

$$2d\sin\theta = m\lambda \quad 1$$

where θ is the incident angle, m is an integer, and λ is the wavelength. The scattered waves satisfy the Bragg condition in equation 1; it called Bragg peak [32]–[34].

Hill et al. demonstrated the first formation of grating on fiber. They observed index variation changes in germane silicate fibers. They fabricated a grating written in the core of the fiber optic. Since $\theta = 90^\circ$, d is the distance between peaks of the interference pattern equation 1 become:

$$2d = m\lambda \quad 2$$

In fiber optic which has grating written in the core, Therefore equation2 become:

$$\lambda_B = 2n\Lambda \quad 3$$

where λ_B is the Bragg wavelength, n is the effective refractive index, and Λ is the period of the refractive index change of the fiber optic. Equation3 is well known

as the Bragg reflection wavelength, the peak wavelength of the narrowband spectral by FBG.

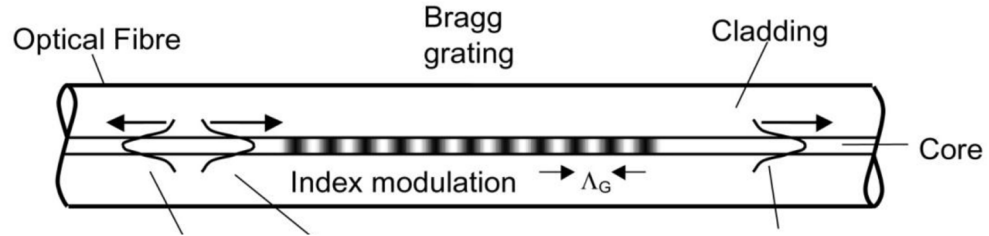


Figure 1. Model of the FBG structure [31].

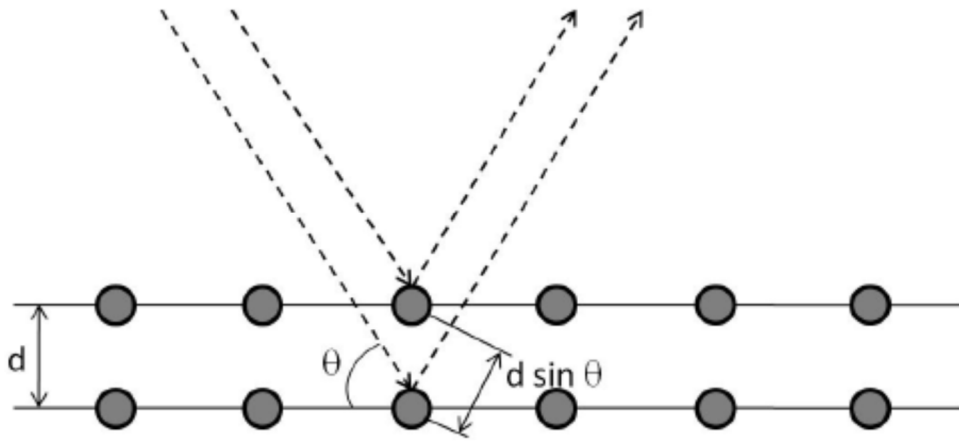


Figure 2. Bragg diffraction on atom lattice [32].

The bandwidth of full width at half maximum (FWHM) of the Bragg reflection in the FBG depends on several parameters, especially the length of the grating. For sensor applications, a typical bandwidth of FBG is 0.05 to 0.3 nm. The bandwidth of FBG can be defined as equation 4:

$$FWHM = \lambda_B S \left\{ \left(\frac{\Delta n}{2n_{c0}} \right)^2 + \left(\frac{1}{N} \right)^2 \right\}^{\frac{1}{2}} \quad 4$$

where S is a parameter of the grating (1 for high or 0.5 for weak reflectivity grating) n_{c0} is the refractive index of the unperturbed core, Δn is the modulation strength, N is a number of periods. Then, the amplitude of the reflected Bragg of FBG (ρ) is given by equation 5:

$$\rho = \frac{\kappa \sinh(\sqrt{\kappa^2 - \delta^2} L)}{\delta^2 \sinh(\sqrt{\kappa^2 - \delta^2} L) + i(\sqrt{\kappa^2 - \delta^2}) \cosh(\sqrt{\kappa^2 - \delta^2} L)} \quad 5$$

where

$$L = N \cdot \Lambda \quad 6$$

$$\kappa = \frac{\pi}{\lambda} \nu \overline{\delta n_{eff}} \quad 7$$

$$\delta = \frac{2\pi}{\lambda} \overline{\delta n_{eff}} \quad 8$$

n_{eff} is the effective refractive index. To illustrate the bandwidth of Bragg wavelength in FBG, figure 3 depicts two different values of kL (2 and 8) in the reflectivity spectrum of FBG when $n_{eff} = 1.457$ and $L = 1$ cm.

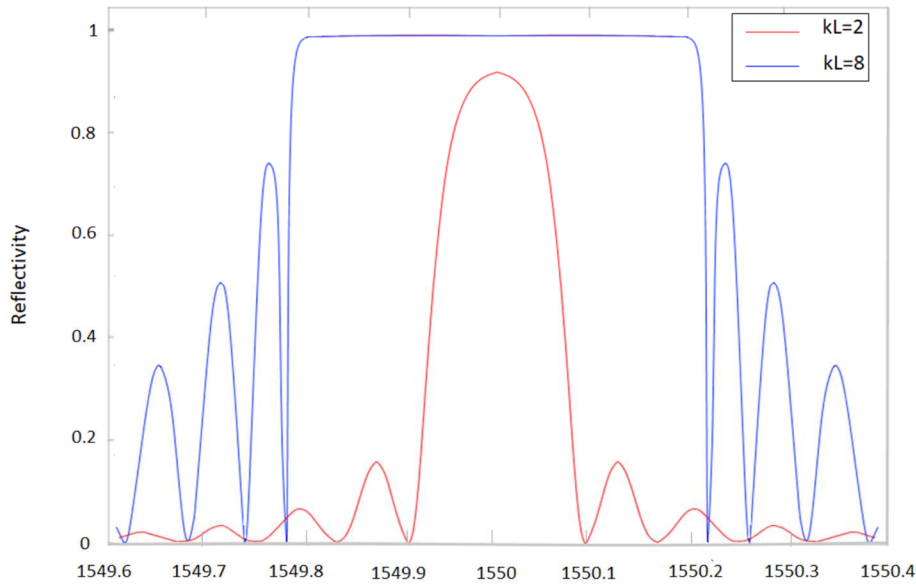


Figure 3. Reflectivity spectrum of FBG for two different values of kL (2 and 8)[35].

2.2 FBG Fabrication Techniques

The first generation FBG was fabricated by employing ultraviolet (UV). Basically, there are two types: photosensitivity and UV laser writing. By using the photosensitivity method, change of the refractive index of silica glass irradiated with high energy UV photon. Typical values for the index change are in the range between 10^{-6} to 10^{-3} , depends on the UV and dopants in the fiber. The second

method, UV laser writing, is based on interference. By using UV laser writing, a small periodic refractive index Λ can be achieved [36], [37].

Besides UV, FBG also can be fabricated by employing ultrahigh peak power radiation from femtosecond pulsed infrared (fs-IR) laser. Now, there are two main categories on how to inscribing Bragg grating with the fs-IR laser. The first category utilizes a specialty phase mask that was precision etched to maximize the coupling of the incident IR laser radiation into the ± 1 orders. The schematic of the first category shows in figure 4(a). The second category utilizes a point to point to write grating within the core region in the fiber by focusing single pulses on the fs-IR, as shown in figure 4(b) [31].

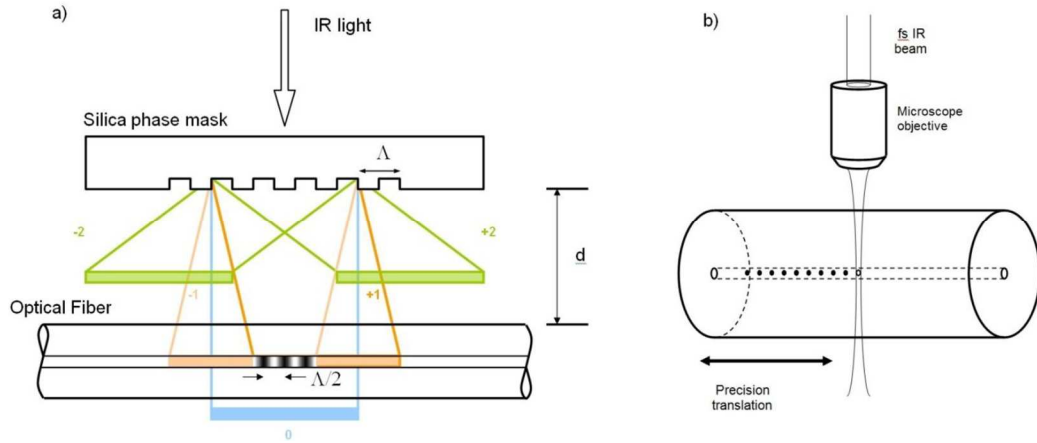


Figure 4. FBG fabrication by using (a) phase mask (b) point to point with fs-IR [31].

2.3 Sensing Principle

Since Bragg wavelength sensitive to temperature and strain, FBG is practically used for environment monitoring. In order to calculate temperature sensitivity only, equation 3 is derived with respect to temperature:

$$\frac{\Delta\lambda_B}{\Delta T} = 2n \frac{\partial\Lambda}{\partial T} + 2\Lambda \frac{\partial n}{\partial T} \quad 9$$

Substituting equation 3 into equation 9, hence we get:

$$\frac{\Delta\lambda_B}{\Delta T} = \frac{1}{\Lambda} \frac{\partial\Lambda}{\partial T} \lambda_B + \frac{1}{n} \frac{\partial n}{\partial T} \lambda_B$$

$$\frac{\Delta\lambda_B}{\lambda_B} = \left(\frac{1}{\Lambda} \frac{\partial\Lambda}{\partial T} + \frac{1}{n} \frac{\partial n}{\partial T} \right) \Delta T \quad 10$$

The first term is the thermal expansion coefficient of silica (ξ_n), and the second term is the thermo-optic coefficient (α_Λ) of the fiber representing the temperature dependence of the refractive index. Substituting two coefficients into equation 10, we obtain:

$$\frac{\Delta\lambda_B}{\lambda_B} = (\alpha_\Lambda + \xi_n) \Delta T \quad 11$$

Then, equation 3 also is derived with respect to displacement in order to get the sensitivity of strain:

$$\frac{\Delta\lambda_B}{\Delta L} = 2n \frac{\partial\Lambda}{\partial L} + 2\Lambda \frac{\partial n}{\partial L} \quad 12$$

Like in temperature sensitivity, substituting equation 3 into equation 12, we get:

$$\frac{\Delta\lambda_B}{\lambda_B} = \left(\frac{1}{\Lambda} \frac{\partial\Lambda}{\partial L} + \frac{1}{n} \frac{\partial n}{\partial L} \right) \Delta L \quad 13$$

Equation 13 could also be written as a function of the strain from material properties of the grating on FBG as the following equation:

$$\frac{\Delta\lambda_B}{\lambda_B} = \left(1 - \frac{n^2}{2} [p_{12} - \nu(p_{11} - p_{12})] \right) \varepsilon \quad 14$$

where p_{ij} is the Pockel's coefficient of the stress-optic tensor and ν is the Poisson's ratio. The equation 14 also can be simplified, so we get expression as given by equation 15.

$$\frac{\Delta\lambda_B}{\lambda_B} = (1 - P_e) \varepsilon \quad 15$$

Combining equation 11 and 15, we obtain the sensitivity of the FBG respect to both temperature and strain:

$$\Delta\lambda_B = \lambda_B [(1 - P_e) \varepsilon + (\alpha_\Lambda + \xi_n) \Delta T] \quad 16$$

Typical parameter FBG for silica fiber with germanium doped core are: $P_e = 0.22$; $\alpha_A = 0.55 \times 10^{-6}/^{\circ}\text{C}$; $\zeta_n = 8.6 \times 10^{-6}/^{\circ}\text{C}$. Thus, typical temperature sensitivity is 14.18 pm/ $^{\circ}\text{C}$ and strain sensitivity is 1.2 pm/ $\mu\epsilon$ [32], [35], [38]. Bragg wavelength shifts due to variation of temperature or strain, as expressed in equation 16 shown as figure 5. Such perturbation in the spectrum is commonly used for sensing applications.

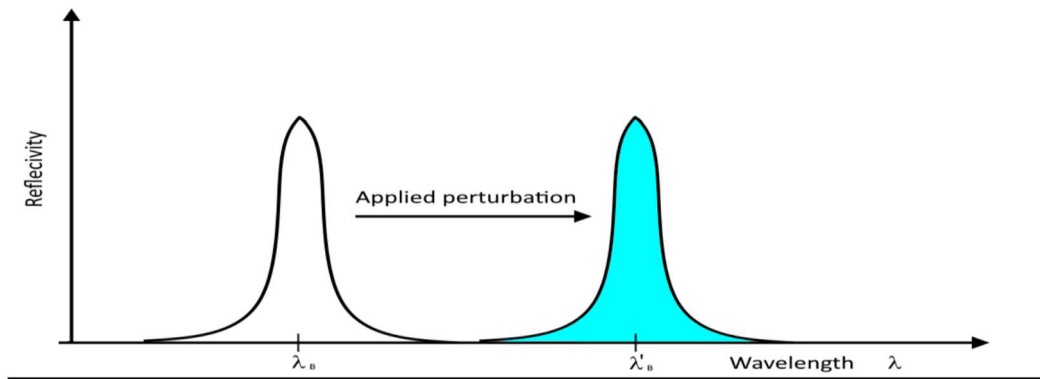


Figure 5. Shift of Bragg wavelength in FBG [35].

Due to the shift of Bragg wavelength is a function of both strain and temperature, cross-sensitivity between them is a problem. By observing only Bragg wavelength, this information cannot explain that the shift of Bragg wavelength is caused by temperature, strain, or both of them. If FBG is desired to measure temperature only, FBG must be protected by strain effect. In this case, FBG can be inserted into small-bore rigid tubing. On the other hand, if FBG is needed to measure strain only, it is rather difficult to protect from the surrounding temperature effect [32]. There are several methods have been reported in order to block temperature effect, such as: introducing a reference FBG, combination with Fabry-Perot interferometer, using superstructure FBG, and coating with polymer material [39], [40].

2.4 Measurement method

Bragg wavelength, as mentioned above, is essential information in FBG, especially when it is employed for sensing applications. Basically, the light inducing in forward through the core of fiber optic, one part is reflected due to

discontinuity at the layer interface, while the other part passes over, as illustrated in figure 6. The reflected part is satisfied with the Bragg condition, as expressed in equation 3.

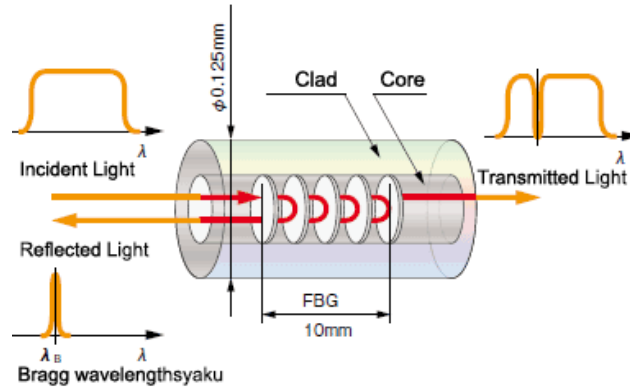


Figure 6. Principle of Bragg wavelength measurement [41].

In the laboratory, the Bragg wavelength shift as shown in figure 6 can be easily measured by using an optical spectrum analyzer (OSA). This measurement method usually uses an amplified spontaneous emission (ASE) as a broadband light source that emits light into fiber optic towards FBG, as shown in figure 7. A back-reflected signal from FBG is passed to OSA to determine the Bragg wavelength. Besides a broad-band light source, the system usually uses a narrowband tunable laser source, as shown in figure 8. Tunable laser source sweeps over spectral in the range Bragg wavelength [42]–[44]. Due to OSA has low scanning speed and high-cost, some researchers proposed alternative methods.

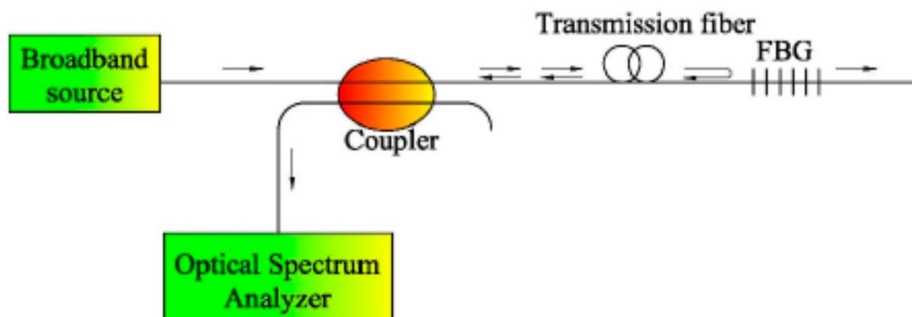


Figure 7. Bragg wavelength measurement by using OSA [44].

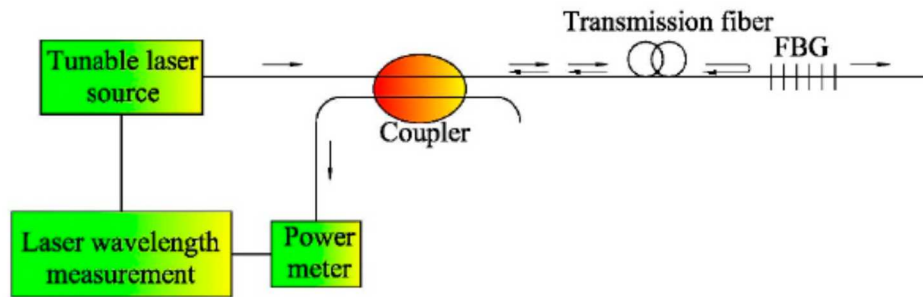


Figure 8. Bragg wavelength measurement by using a tunable laser [44].

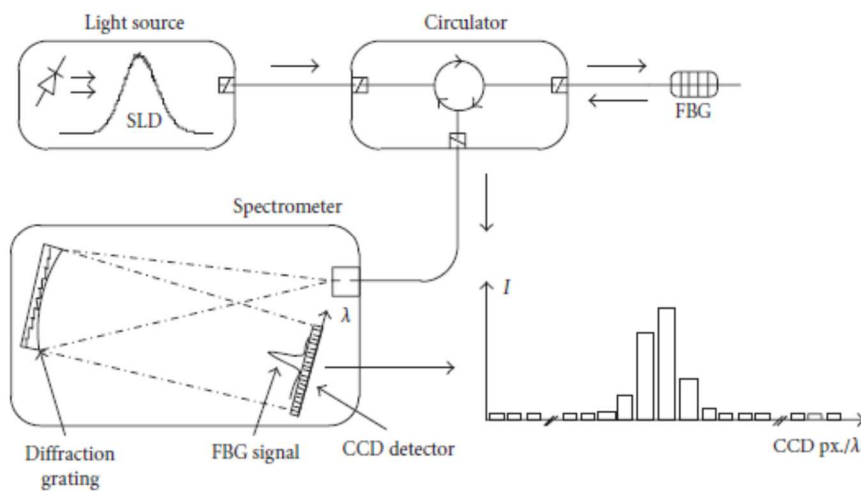


Figure 9. Bragg wavelength measurement by using CCD-spectrum [45].

One of the methods recently developed is a charge-coupled device (CCD) spectrometers. In this technique, light reflected from FBG is spread using dispersive optical components such as prisms or diffractive gratings onto CCD line arrays, as shown in figure 9. CCD in this system is required to monitor the position of the peak wavelength in the reflection spectrum, which expresses the physical parameter change. The CCD-spectrometer based interrogation is limited by the number of the pixel resolution of the detector. A typical CCD has a 256 detector pixel with a wavelength range of 45 nm (1525-1570 nm), corresponds to 0.17 nm resolution [11], [45].

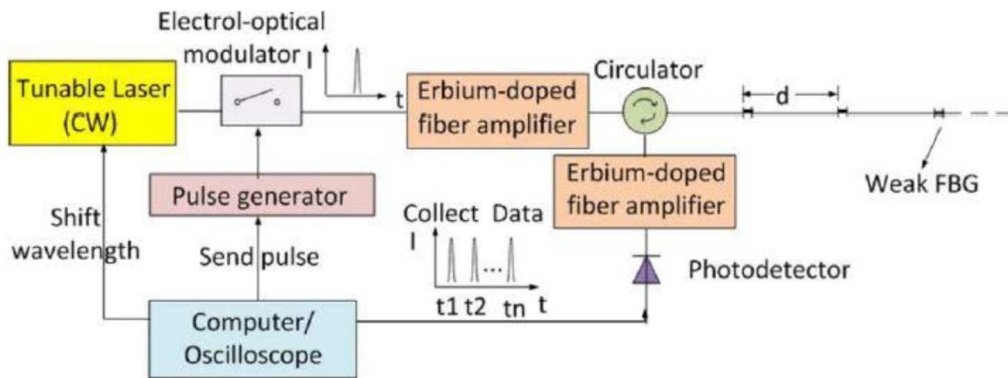


Figure 10. Bragg wavelength measurement by using TDM [46].

The challenge method of how to interrogate FBG is multiplexing issue FBG sensors due to the complexity needed in applications. Multiplexing is a method of how to use only one light source and detector to explore multiple discrete sensors. One of the methods that are possible to be implemented to multiplexing FBG is a time-division multiplexing (TDM) and wavelength-division multiplexing (WDM). In TDM, the time of flight with sort duration is used to recognize a reflected signal from FBG through propagation time delay. Multiplexed FBG measurement based on TDM is illustrated in figure 10 [14], [24], [44], [46]. An electro-optical modulator modulates the continuous wave of the tunable laser, and then laser emits to array FBG through one optical fiber. The individual FBG is separated by the time of arrival of a particular peak wavelength. The other way, WDM, a broadband light source is emitted into series FBG, as shown in figure 11. Reflected light from each FBG is separated by wavelength division using a dispersive element, such as a grating or prism [47].

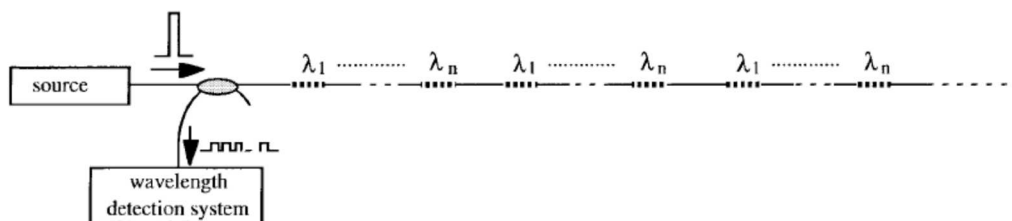


Figure 11. Bragg wavelength measurement by using WDM [47].

Other researchers also reported a multiplexing FBG could be carried out by employed two-photon absorption (TPA) methods, as shown in figure 12. TPA is the absorption of two photons of identical or different frequencies in order to excite from ground state to higher state. This method usually uses silicon photodiode or avalanche photodiode. Two lasers with different wavelengths are used for probe and reference, which are modulated with same frequency (f_m). The probe laser is also modulated by frequency (f_L). The reflected signal from FBG is combined with the reference signal. Due to the optical path length difference between reference and FBG, positions each FBG can be identified [48].

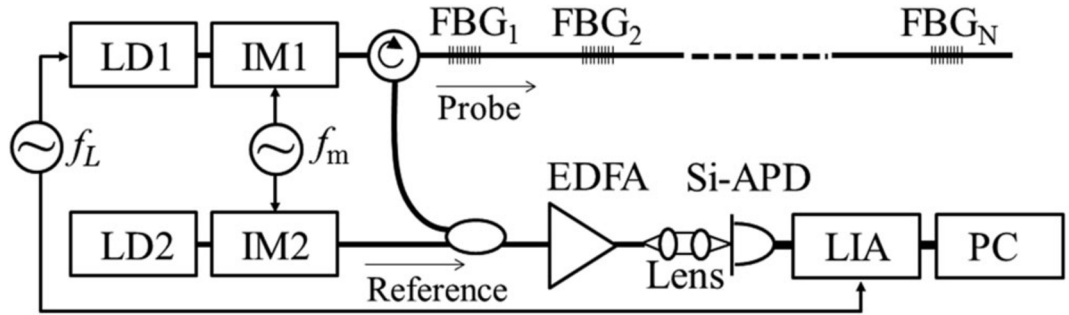


Figure 12. Bragg wavelength measurement by using TPA [48].

Then, the possible method in multiplexing FBG interrogation utilizes the optical time-domain reflectometry (OTDR). This technique has established since 1980 as an investigator for the fiber-optic network. In principle, a short pulse is launched into FBG; due to reflectivity on the grating of FBG, a tiny fraction of light will be backscattered and then analyzed. This process can be illustrated in figure 13. The pulse of light travels for time $t = z/v$ a long fiber optic to reach an FBG at distance z from the source. Due to $v = c/n$, after reflecting from the grating, the scattered light backscattered to reach the front end of the fiber optic again for $t_d = 2nz/c$. So, location of FBG can be defined by equation 17:

$$z = \frac{c}{2n} t_d \quad 17$$

And, the smallest distance between two FBG is given by equation 18:

$$\Delta z = \frac{c\tau}{2n} \quad 18$$

τ come from pulse width, therefore in order to achieve good the spatial resolution, the pulse has to be reduced [27], [49], [50].

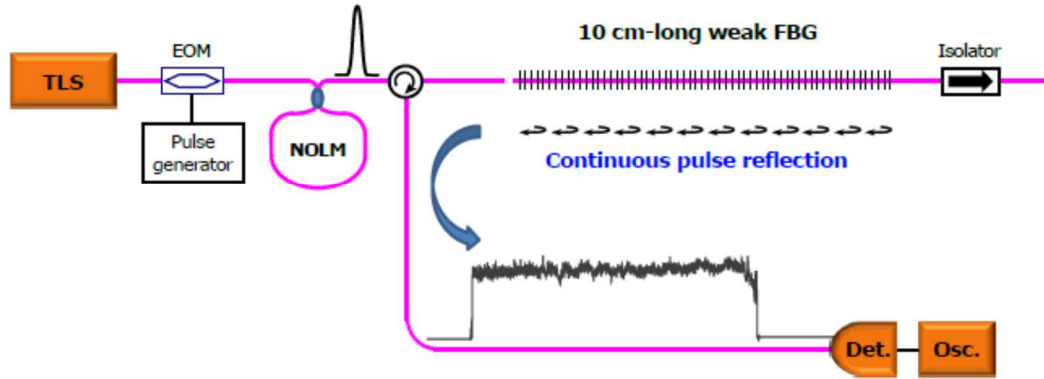


Figure 13. Bragg wavelength measurement by using OTDR [49].

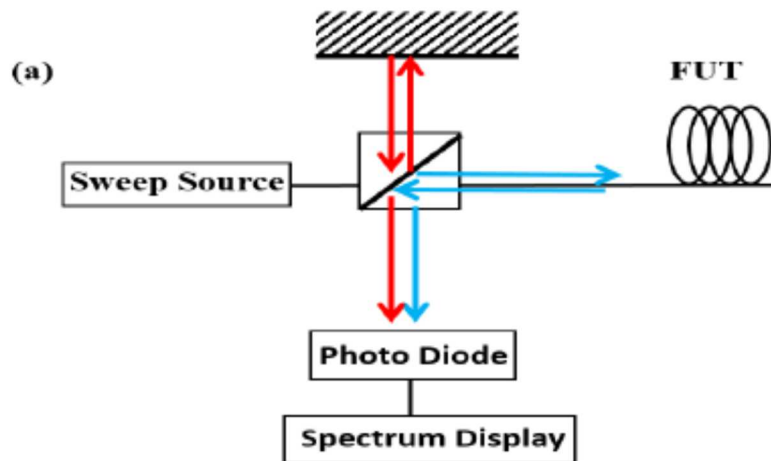


Figure 14. Bragg wavelength measurement by using OFDR [51].

Beside time-domain reflectometry, optical frequency domain reflectometry (OFDR) is now widely used to interrogate multiplexing FBG sensors. OFDR has all capabilities as OTDR but with higher resolution and better sensitivity. Instead of a pulse source, a source in OFDR is used a linearly swept in time with frequency sweep time (T_s), sweep span (ΔF), and sweep rate (γ) as expresses in the equation 19:

$$\gamma = \frac{\Delta F}{T_s} \quad 19$$

Then, the linearly swept signal is splitted into two signals probe signal and a reference signal. After that, the probe signal is transmitted to a target, and the reflected signal from the target is combined with the reference signal. The combined signal produces a constant beat frequency corresponding to the location of the target as defined in equation 20:

$$f_B = \gamma \cdot 2L \frac{n}{c} \quad 20$$

where f_B is the beat frequency and L is the distance of a target. OFDR is categorized into coherent OFDR (C-OFDR) and incoherent OFDR (I-OFDR). The first category, C-OFDR, a probe signal and a reference signal are combined coherently, as shown in figure 14. It requires a coherent optical light source with a narrow linewidth. The second category, I-OFDR, a signal is processed by vector network analyzer (VNA) or electronic mixing [10], [27]–[30], [51], [52]. A subgroup of I-OFDR called Frequency-Modulated Continuous Wave (I-FMCW) would be used in our proposed system. This method will be described in Chapter 4.

2.5 Peak of Bragg wavelength tracking

In order to analyze the spectrum of the FBG, which is shown in figure 3, it is necessary to be defined as the FBG peak wavelength. Thus, the estimated Bragg wavelength is useful in estimating physical parameters like strain or temperature. Recently, several peak-tracking methods have been proposed for estimating Bragg wavelength as following:

a. Direct methods

There are three kinds of direct methods, such as maximum, X-dB bandwidth, and centroid method. The maximum direct method estimates the peak Bragg wavelength from wavelength at which the maximum reflectivity. The X-dB bandwidth direct method approaches the Bragg wavelength, which is estimated as the center of the inner bandwidth. The X value is often to set in 3 dB. The X-dB bandwidth method is illustrated

in figure 15, and the operational to calculate Bragg wavelength is defined as follows:

$$\lambda_B = \min(\lambda_{th}) + \frac{\max(\lambda_{th}) - \min(\lambda_{th})}{2} \quad 21$$

The third direct method, the centroid method determines the Bragg wavelength as a center of mass of the reflection spectrum of FBG, as shown in figure 16. Compared to other methods, the centroid has high precision and more robust than others when the noise of raw data is processed. A simple algorithm easily calculates this method as express in equation 22:

$$\lambda_B = \frac{\sum_{i=1}^N \lambda_i \cdot M_i}{\sum_{i=1}^N M_i} \quad 22$$

where λ_i is the wavelength of the VCSEL at the i -th point, and M_i is the magnitude of beat frequency at the i -th point. Then, λ_B can be defined by integration using equation 22 from $i = 1$ to N , where N is the number of data whose magnitude M_i is higher than a given threshold shown as a dashed line in figure 16.

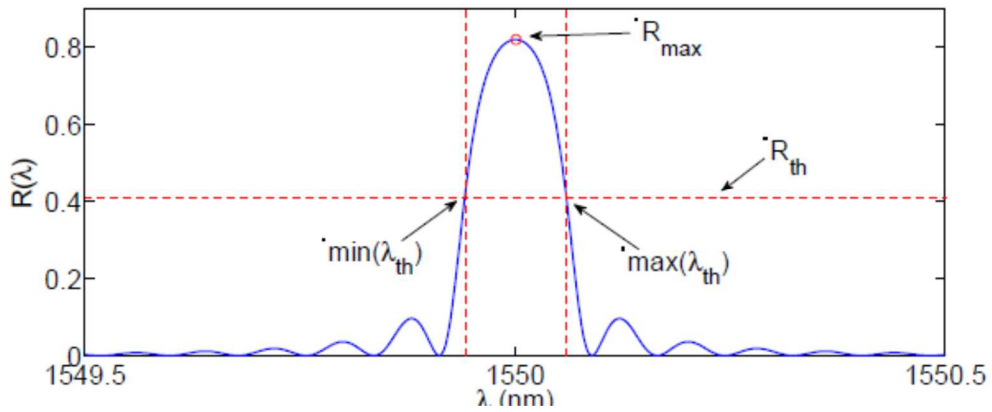


Figure 15. Peak tracking by X-dB bandwidth method [53].

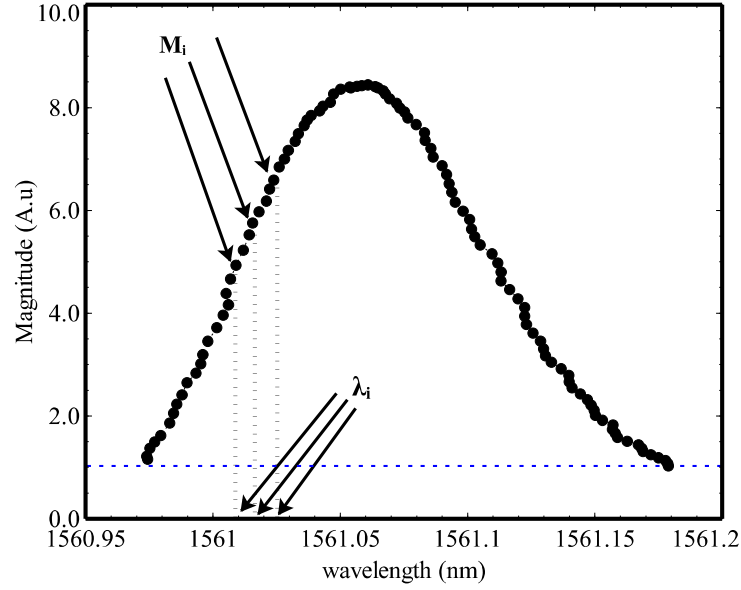


Figure 16. Peak tracking by centroid method.

b. Curve fitting method

FBG spectrum is interpolated with a function that approximates its shape. In these methods, there are two kinds of operations:

- 2nd order polynomial: this operation can be performed by using a least-squares interpolation based on quadratic regression, as shown in figure 17. The Bragg wavelength can be estimated by equation 23:

$$R(\lambda) \approx a_2\lambda^2 + a_1\lambda + a_0 \quad 23$$

Determining a_0 , a_1 , a_2 can be performed by using a least-squares interpolation method based on quadratic regression.

- Gaussian polynomial Fit

This method is approximated as a Gaussian function, as expressed in equation 24 and figure 18.

$$\ln[R(\lambda)] \approx \frac{1}{2\sigma^2}\lambda^2 + \frac{\lambda_0}{\sigma^2}a_1\lambda + (\ln A - \frac{\lambda_0^2}{2\sigma^2}) \quad 24$$

Basically, this method is slightly same with 2nd order polynomial.

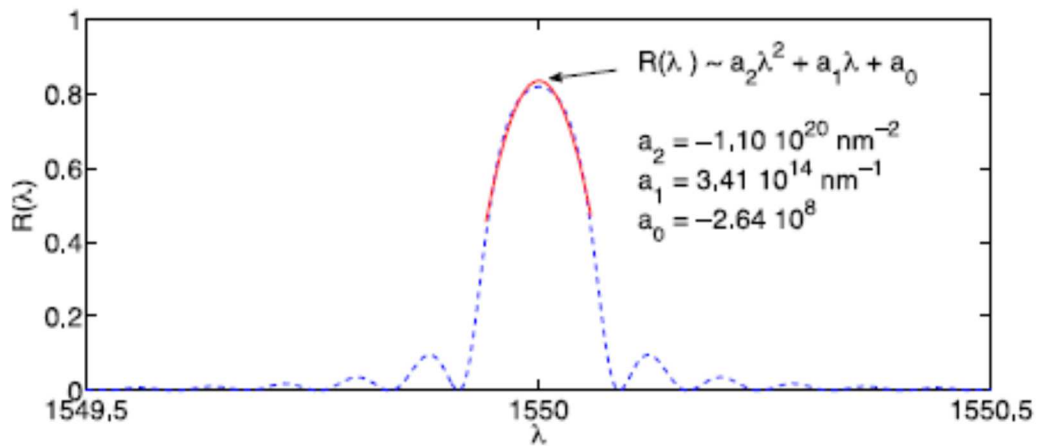


Figure 17. Peak tracking by 2nd order polynomial [53].

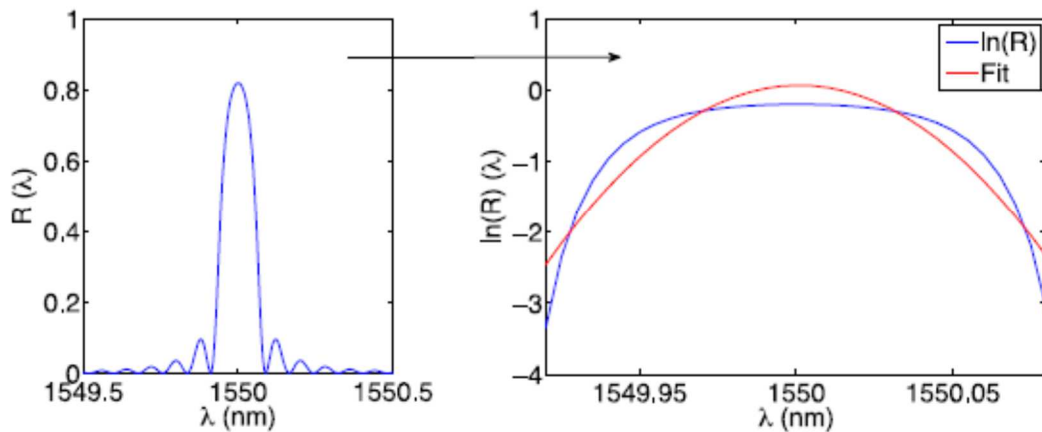


Figure 18. Peak tracking by Gaussian polynomial fit [53].

c. Correlation

This method is calculated by a mutual correlation between the measured spectrum and the reference spectrum. These techniques have several kinds, such as wavelength-shifted mutual correlation, cross-correlation, and correlation polynomial fit [53]–[55].

2.6 FBG measurement

We then experimented with measuring the Bragg wavelength of FBG by using a broadband light source and OSA, as illustrated in figure 7. We conduct the FBG sensor measurement to recognize temperature and strain. The result of a

measurement can be shown in figure 19 and figure 20. The horizontal axis represents the temperature in degree Celcius for figure 19, and strain in microstrain for figure 20. The vertical axis represents the Bragg wavelength for both figures. Figures 19 and 20 show Bragg wavelength linearly changes as a result of temperature or strain change. These results also give information that temperature and strain sensitivity of this FBG: 17.6 nm/°C, 0.3 pm/με, respectively.

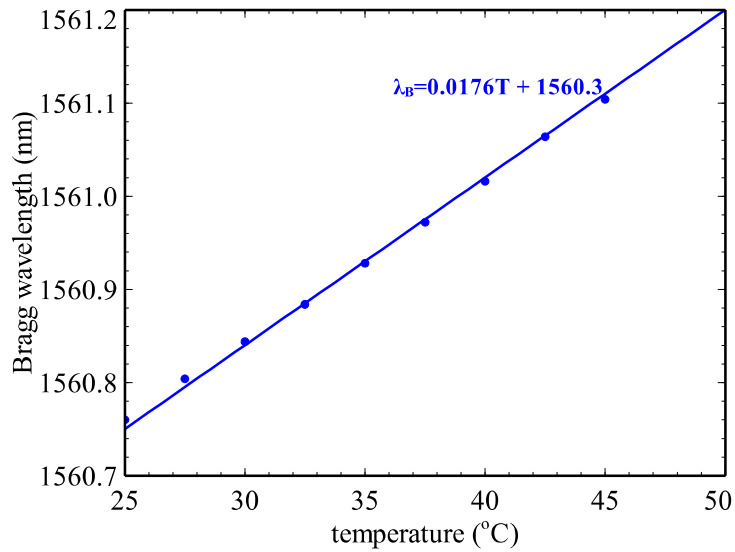


Figure 19. Temperature sensing measurement by using FBG sensor.

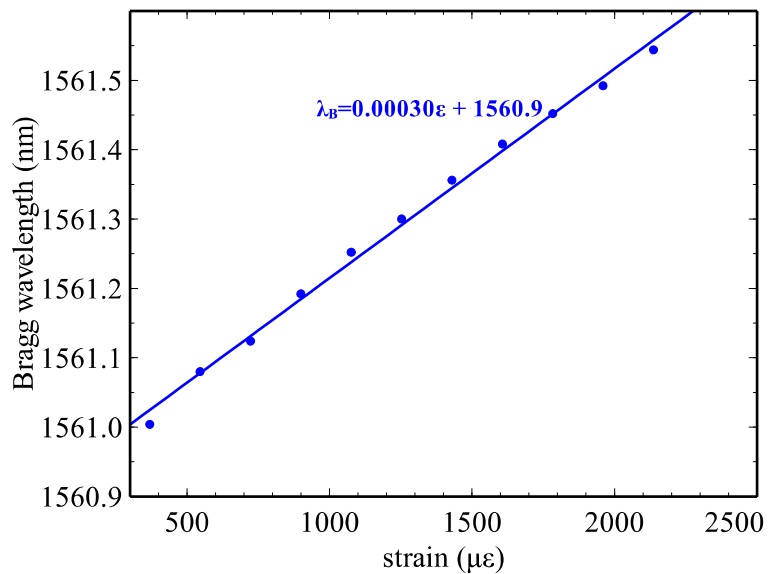


Figure 20. Strain sensing measurement by using FBG sensor.

2.7 Summary

In Chapter 2, we have briefly explained the FBG structure and sensing principles. This fiber has a unique configuration in the core, usually called a grating. The important parameter of FBG is the Bragg wavelength, which represents the measurand information. Due to FBG sensitive to strain and temperature change, the FBG sensor becomes popular in SHMS applications. Several ways to evaluate Bragg wavelength have been introduced with their strengths and weakness. Since SHMS requires not only one point but also a long-range area, I-FMCW has a possibility for developing an FBG interrogator for the purpose of long-range SHMS and multi-point sensors.

Chapter 3: VCSEL

3.1 Structure of VCSEL

The vertical-cavity surface-emitting laser (VCSEL) was invented by Prof. Kenichi Iga in 1977. VCSEL is a type of laser diodes with a very short cavity ($\sim 1 \mu\text{m}$) and a very thin active region between two distributed Bragg reflectors (DBR), as shown in figure 21. The reflectors are formed by quarter-lambda thick epitaxy layers (d) with alternating high and low refractive indices as expressed in equation 25:

$$d = \frac{\lambda}{4n} \quad 25$$

The active region consists of multiple quantum wells (MQW) in the center of a full or half lambda thick cavity layer. Full or half lambda depends on the refractive index of the cavity layer and DBR. The light travels in the vertical direction back and forth between DBR. If a specific wavelength fulfills the phase condition, a laser emits a coherent wavelength. Due to the vertical nature of emitted light, the entire two-dimensional array of VCSELs can be tested without separation of lasers. As a result, cost of production of VCSELs lower than an edge-emitting laser [20], [21], [23], [56], [57].

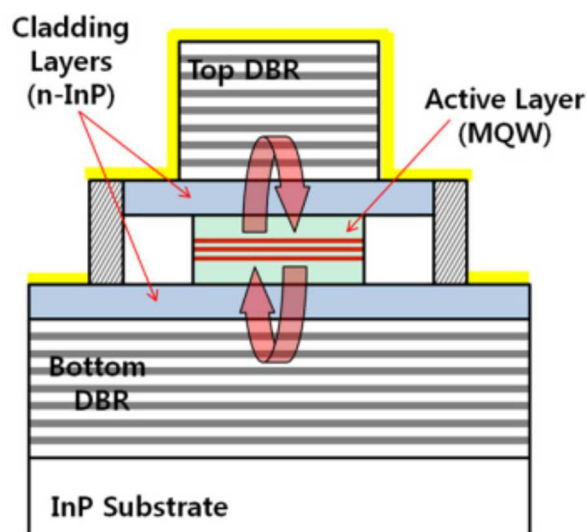


Figure 21. Structure of VCSEL [21].

Both of Bragg reflectors at VCSELs consist of alternating layers of semiconductors with different bandgaps, such as GaAs and $\text{Al}_x\text{Ga}_{1-x}\text{As}$. Bragg reflectors at VCSEL have very high reflectivities of more than 99% in order to support the necessary feedback needed for lasing. The reflectivity can be adjusted by index x $\text{Al}_x\text{Ga}_{1-x}\text{As}$ and the thickness layer [50]. Figure 22 shows a typical DBR in VCSEL with a sequence of mirror pairs that have refractive indices n_1 and n_2 , n_s are the refractive index of the substrate, and n_m is the refractive index of mirror ends into a medium. Amplitude (ρ) and power reflectivities (R) for Bragg wavelength at the center of the stop-band can be calculated by using equation 26 and 27:

$$\rho = \pm \frac{r(n_M+n_2)-(n_M-n_2)}{(n_M+n_2)-r(n_M-n_2)} \quad 26$$

$$R = \frac{\left(\frac{n_2}{n_1}\right)^{2N} - \frac{n_2}{n_s}}{\left(\frac{n_2}{n_1}\right)^{2N} + \frac{n_2}{n_s}} \quad 27$$

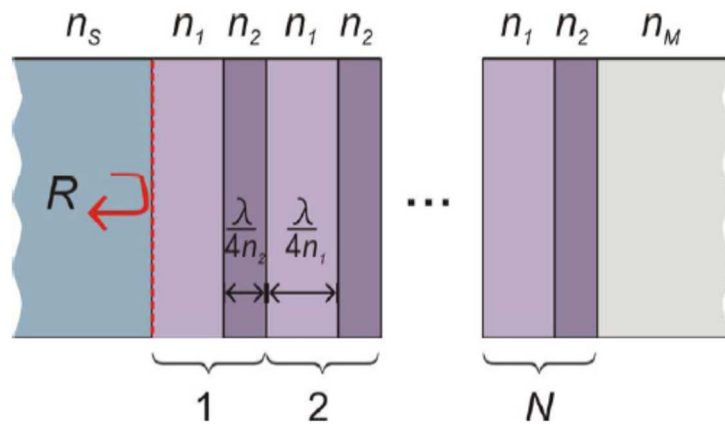


Figure 22. DBRs structures in VCSEL [23].

VCSEL offers many kinds of advantages when compared to others so that many applications in the fiber-optic network. VCSEL has compatibility with low-cost wafer-scale fabrication and testing methods. Beside low-cost, VCSEL also offers several attractive characteristics such as high modulation bandwidth (>10 GHz), single-mode operation, low power, potential for producing integrated

modules, high efficiency, low threshold current (<1 mA) [50], array on wafer [58], and very low relative intensity noise (RIN) [18]. In semiconductor laser, like VCSELs, a noise is dominated by spontaneous emission [57].

Current through DBRs, which is doped by a semiconductor, is injected into the active region simply and most uniform. Due to doping semiconductor mirrors for increasing current transport, the optical loss mirrors also increase, which limits the peak reflectivity. Therefore, it must be a balance between high reflectivity and low electrical resistance. The voltage is determined by the resistance of each mirror period and the potential difference in each heterojunction barrier. The resistance of p-type DBRs is higher than n-type DBRs.

The active region has a role in determining a wavelength that will emit in VCSEL. A recent development, the active region materials, is design for commonly used in the range of 1.3 – 1.55 μm . For this reason, active regions are usually used material from Indium Phosphide-Indium Gallium Arsenide Phosphide (InP-InGaAsP). Long-wavelength lasers are typically packaged with thermoelectric cooler in order to mitigate the inherent temperature sensitivity [58].

3.2 Theory of VCSEL

As usual diode laser, light is amplified by the gain medium between mirrors. Two mirrors partially reflect the light, so it bounces back and forth through the gain medium. If the gain is enough, the laser will emit a coherent light [59]. In order to obtain VCSEL with wavelength (λ), the cavity and active region have to be required a condition as following:

$$E = \frac{hc}{\lambda} \quad 28$$

where h is the Plank's constant (6.62×10^{-34} J.s), and $E = E_{gs} + E_c + E_v$; E_{gs} is bandgap energy of the strained quantum wells region, E_c is the energy of conduction band, and E_v is the energy of valence band. E_c and E_v can be expressed in equation 29 and 30, respectively:

$$E_c = \frac{\hbar^2}{8m_c} \quad 29$$

$$E_v = \frac{h^2}{8m_v l_w^2} \quad 30$$

where l_w is the thickness of the quantum well, m_c and m_v are the effective masses of the electron in the conduction band and the valence band, respectively [60].

The emission wavelength (λ) of VCSEL is determined by resonance condition as written in equation 31:

$$\langle \bar{n} \rangle L = \frac{m\lambda}{2} \quad 31$$

where \bar{n} is spatially averaged refractive index, m is a positive index, and L is an inner cavity of length. Since splitting of the active region into segments separated by $\lambda/(2\langle \bar{n} \rangle)$ has to be avoided for the efficiency of carrier injection, and the shortest symmetric cavity is one wavelength thick, equivalent to $m = 2$.

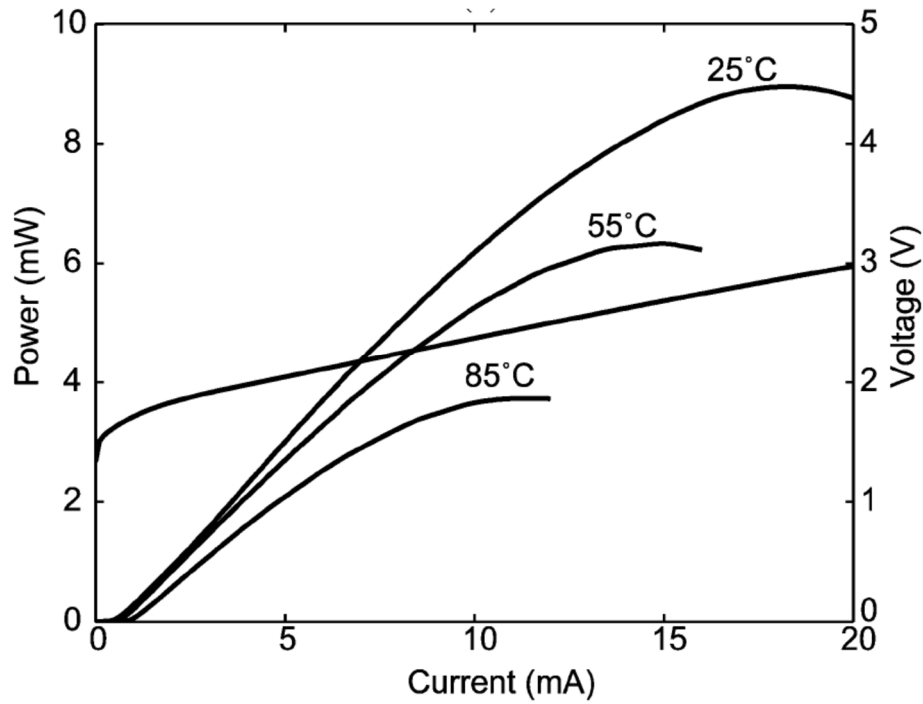


Figure 23. Light-current-voltage curve of VCSEL [61].

The optical power output of VCSEL can be calculated by equation 32:

$$P = \eta_i \eta_0 \frac{hc}{\lambda q} (I - I_{th}) \quad 32$$

where η_i is injection efficiency, η_o is optical efficiency. Figure 23 shows the typical light-current-voltage curves of VCSEL. The x-axis represents the current injected into VCSEL, the right ordinate is the voltage across the VCSEL, and the left ordinate is optical power emitted [61].

The conversion efficiency (η) for emission through top and bottom reflector is defined as the ratio of coherent light output power (P) and electrical input power, as expressed in equation 33:

$$\eta = \frac{P}{IV} \quad 33$$

where I is injected current, and V is the voltage applied across the VCSEL. Efficiency is maximum when injected current (I_c):

$$I_c = I_{th} \cdot (1 + \sqrt{1 + \xi}) \quad 34$$

$$\xi = \frac{V_k}{I_{th}R_s} \quad 35$$

I_{th} is threshold current, V_k is kink voltage that is related to the separation of the quasi-Fermi energies, which approximated by $V_k \approx \bar{h}/\omega/q$, \bar{h}/ω is photon energy, q is the electron charge, and $R_s = dV/dI$ denote the differential series resistance [62].

The emission wavelength is determined by the cavity resonance and not by the gain peak as in Fabry-Perot lasers. Therefore, the wavelength shift is governed by changes in the average refractive index in the resonator and about 10% by thermal expansion of the semiconductor layers [62]. For VCSELs in the range, 800 – 1000 nm and in the range 1500 – 1600 nm have mode shifts typically in $\frac{\partial \lambda}{\partial T} \approx 0.07$ nm/K and 0.08 nm/K, respectively [21].

The spectral power density of the single-mode laser emission line can be approximated by the Lorentzian lineshape function, which is given by equation 36:

$$|\tilde{E}(v)|^2 = |\tilde{E}(v_m)|^2 \frac{\left(\frac{\Delta v_L}{2}\right)^2}{\left(\left(\frac{\Delta v_L}{2}\right)^2 + (v - v_m)^2\right)} \quad 36$$

with ν_m is the center frequency of the mode and $\Delta\nu_L$ is the full linewidth at half maximum, which is given by equation 37:

$$\Delta\nu_L = \frac{\bar{\beta}_{sp}\Gamma\langle n_w \rangle}{4\pi\tau_{sp,w}\langle N \rangle} (1 + \alpha_H^2) \quad 37$$

where α_H is the linewidth enhancement factor (typically takes a value between -2 and -7), $\Gamma\langle n_w \rangle$ is confinement factor from carriers of densities in the active region, N is photon density, and $\tau_{sp,w}$ is spontaneous emission time [62].

3.3 Tunable wavelength of VCSEL

VCSEL can be designed as swept wavelength in many ways, including DBR mirror design, MEMS structure and tuning mechanism, current confinement, cavity design, and pumping mechanism. A swept wavelength by manipulating DBR mirror design can be accomplished by applying a reverse bias voltage between DBRs. This generates electrostatic force, which attracts the top DBR downward toward the substrate. As a result, the optical length of the laser cavity change and thus produces a shift of wavelength. By using MEMS structure and tuning mechanism, a swept wavelength can be provided by utilizing dielectric DBR mirrors such as a larger index difference, shorter effective cavity length, and larger free spectral range (FSR).

VCSEL may provide a way of making swept-source by simply temperature and injection current tuning without internal and external elements that are involved. Due to DBRs have poor thermal conductivities, if internal heat sources easily increase the temperature of the active region. In this case, when more injected current is injected, the internal temperature of the active region is also getting higher. This effect is called the self-heating. As a result, the temperature change in the active region produces a shift of operation wavelength.

When a sawtooth current drives VCSEL, the output response of the VCSEL is shown in figure 24. The temperature gradually increases, and the wavelength is continuously swept accordingly. This gives a suitable VCSELs to make a self heating-induced sweep. In another case, when VCSEL is driven by DC injected current, the output response of the VCSEL is shown in figure 25.

This figure shows the spectra when injected current $I = 2, 4, 6, 8, 10,$ and 12 mA. The peak of spectra is clearly shown if the injected current on VCSEL is changed [21].

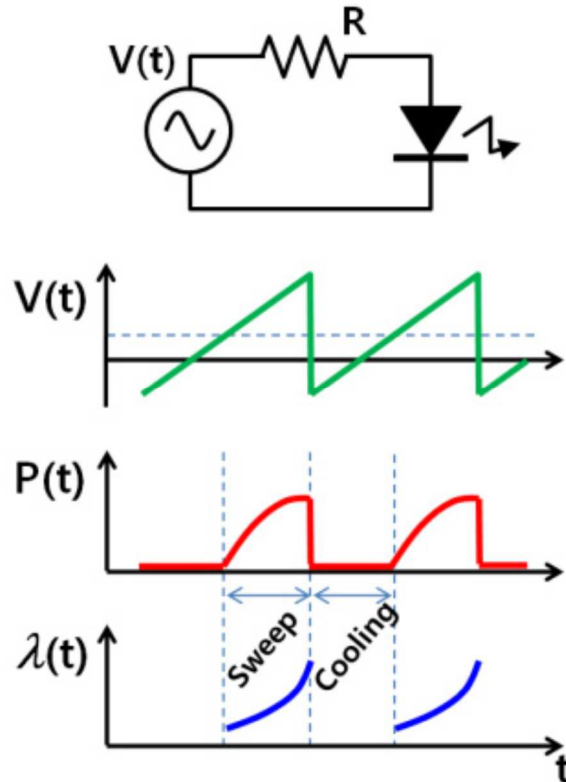


Figure 24. Injected current scheme and output response of VCSEL [21].

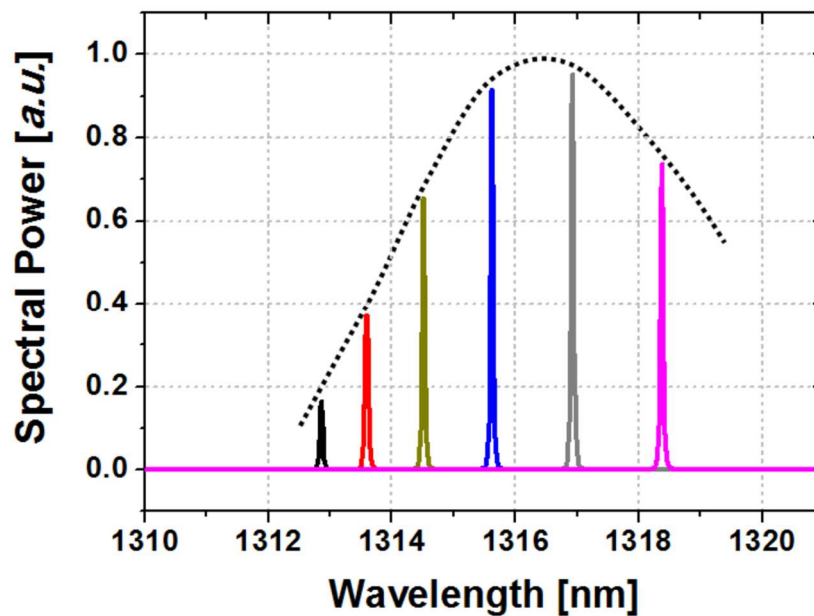


Figure 25. Wavelength change as a result of injection current on VCSEL[21].

Recently, many advances in research and fabricated on VCSEL. Now, we can meet multiple wavelengths on the monolithic integration of the module, which is a VCSEL array. The illustration for multiple-wavelength VCSEL can be understood as following:

- a. Fabry-Perot (FP) wavelength within the gain spectrum is only one and lasing wavelength is determined by FP wavelength.
- b. Optical thickness variation of the layers changes FP wavelength and lasing wavelength.
- c. The position of the layers with thickness variation is crucial to define wavelength variation [63]

3.4 Modulation of VCSEL

VCSEL is able to be modulated directly (internal modulation) or indirectly (external modulation) for generating frequency-modulated light. Direct modulation on VCSEL is based on modulation of the optical resonator in the VCSEL such as length of the optical resonant cavity, a refractive index of the medium in the cavity, or combination of length and refractive index in a cavity as expressed in equation 38 and 39 [64]:

$$\Delta\lambda_k = \frac{\lambda_k \Delta L}{L} \quad 38$$

$$\Delta\lambda_k = \frac{\lambda_k \Delta n}{n} \quad 39$$

This technique can be realized by introducing a bias T circuit that drives the VCSEL, as illustrated in figure 26. However, it is limited by the characteristic of the laser itself; it causes reducing the operational lifetime of VCSEL [59], [65]. Indirect modulation involves electro-absorption (EA) modulators; usually, a semiconductor material that provides the modulation. Indirect modulation on the laser can be illustrated in figure 27. EA modulator, which usually used in this method, is an electro-optical modulator [66].

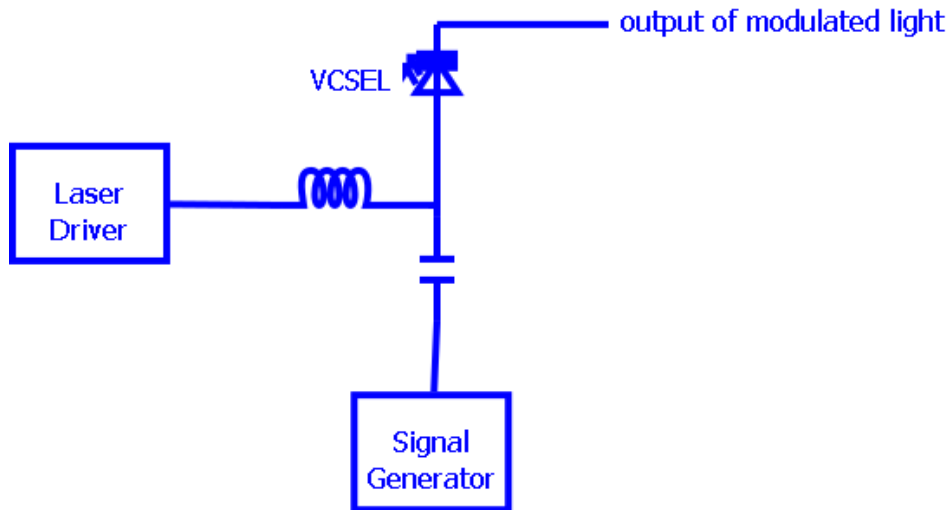


Figure 26. Bias T circuit for direct modulating a VCSEL.

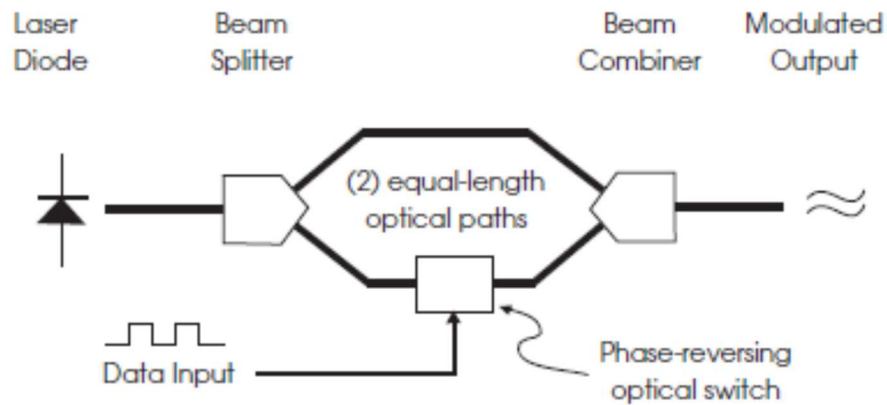


Figure 27. External modulation on VCSEL by using modulator [65].

The frequency modulation response of VCSEL for different bias current is shown in figure 28. laser 3-dB bandwidth and frequency response damping increase as the bias current until certain value. The frequency response can be modeled as:

$$H(\omega) = \frac{\omega_R^2}{\omega_R^2 - \omega^2 + j\omega\gamma} \quad 40$$

where ω_R is relaxation resonance frequency and γ is a damping factor which is defined by equation 41 to 44:

$$\omega_R^2 = \frac{v_g a N_p}{\tau_p} \quad 41$$

$$\gamma = K f_R^2 + \gamma_0 \quad 42$$

$$K = 4\pi^2 \tau_p \left(1 + \frac{\Gamma a_p}{a}\right) \quad 43$$

$$\gamma_0 = \frac{1}{\tau \Delta N} + \frac{\Gamma \beta_{sp} R_{sp}}{N_p} \quad 44$$

v_g is group velocity, $a = \delta G / \delta N$ is the differential gain, K is K factor, $a_p = \delta G / \delta N_p$, γ_0 describes the damping of the laser response, $\tau \Delta N$ is the differential carrier lifetime. To achieve high-speed frequency modulation, some parameters in VCSEL can be modified such as increasing relaxation resonance frequency and reducing photon lifetime [66].

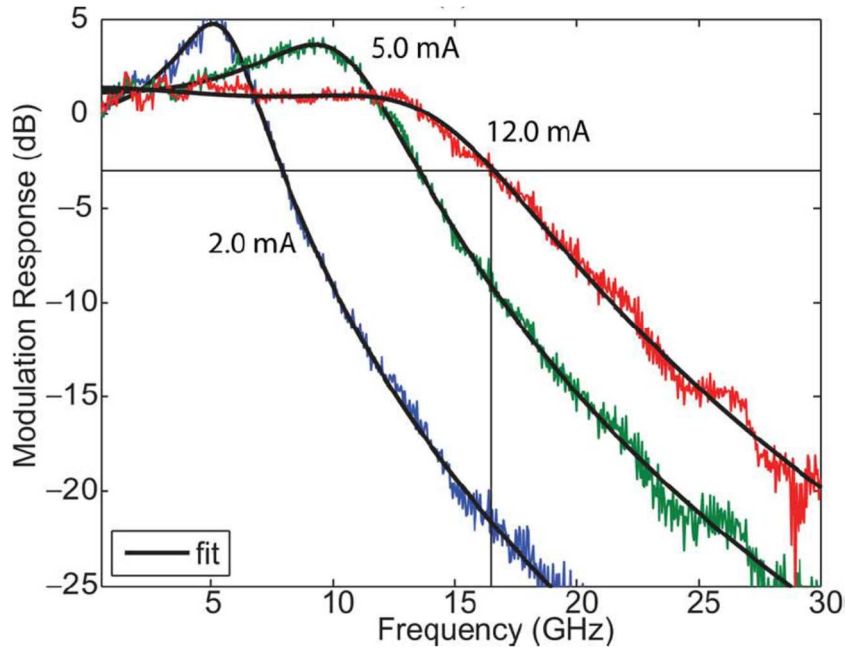


Figure 28. Frequency modulation response of VCSEL for different bias current[61].

3.5 Measurement of VCSEL wavelength

As explained in section 3.3, the variation wavelength of the VCSEL can be tuned by simply injection current change. Then, we measure a wavelength sweep of VCSEL by injection current change as illustrated in figure 29. In the first

experiment, we want to know the effect of different temperatures on the case of VCSEL for tunable wavelengths. The result of the measurement is shown in figure 30. The horizontal axis represents the injection current to VCSEL in mA, and the vertical axis represents the wavelength of the VCSEL. The result shows that different temperatures in the case of VCSEL influence the wavelength, which is resulted. In order to make stable for generating wavelength sweep in our experiment, we then should control the temperature of the case of VCSEL. In our proposed system, we control the temperature of VCSEL to 20 °C. The result is shown in figure 31. The obtained relationship between the injection current and the wavelength is $\lambda \text{ (nm)} = 0.5696 \text{ ILD (mA)} + 1557.3$, where ILD is the injection current of the VCSEL. Then, this relation will be stored in the program developed in Chapter 5 and is used to define the wavelength of the VCSEL.

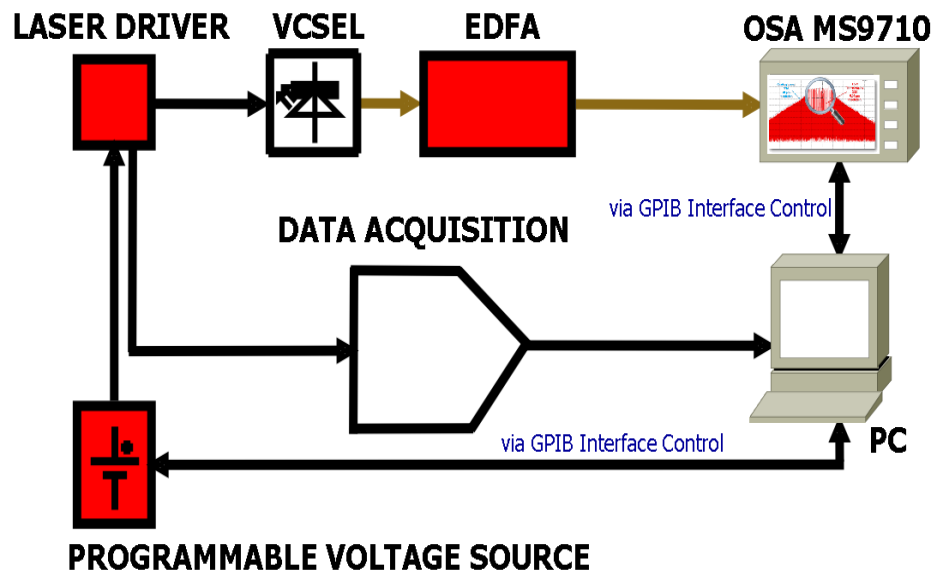


Figure 29. Set up the measurement of a shift of VCSEL wavelength by using injection current.

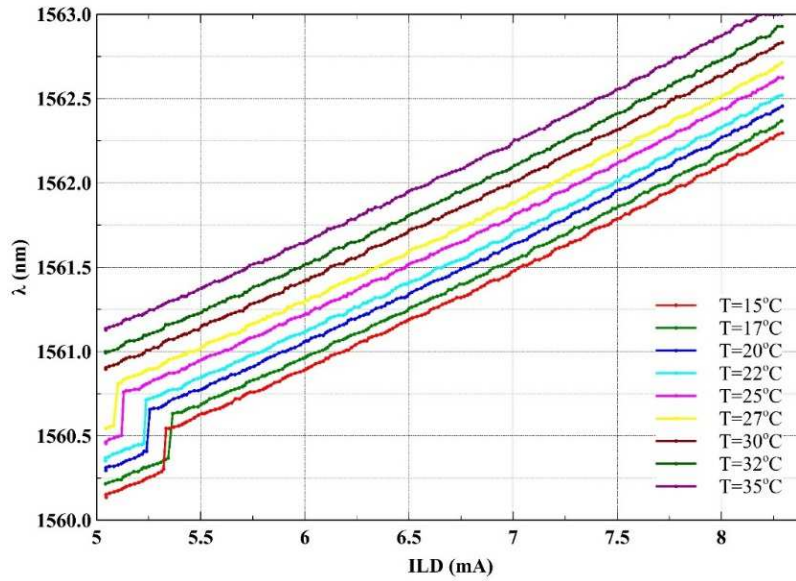


Figure 30. Influence of VCSEL case temperature change in wavelength shift.

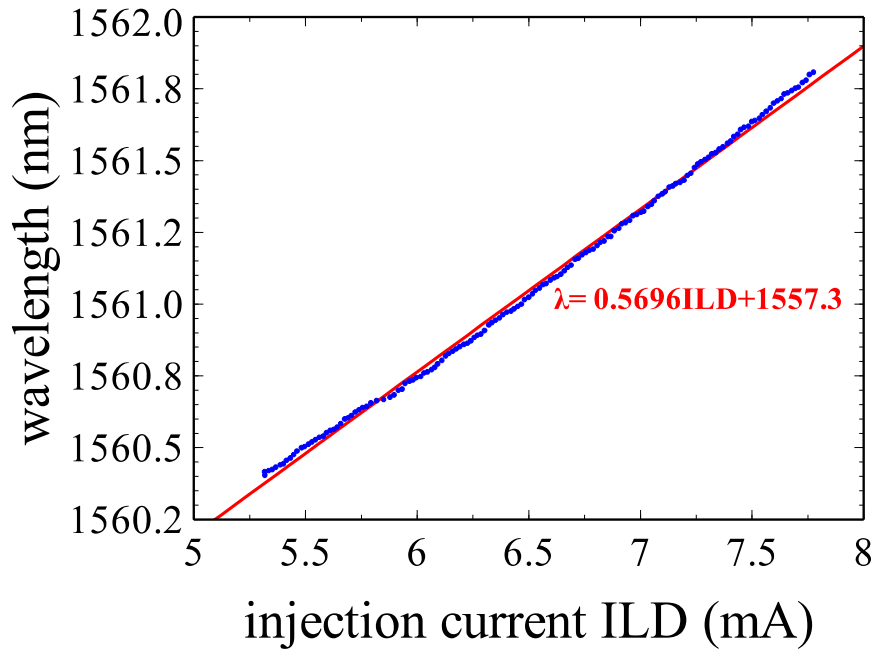


Figure 31. Correlation between injection current on VCSEL with wavelength, with the temperature of VCSEL case 20°C.

3.6 Summary

VCSEL, a low-cost diode laser, has a promising feature for tunable wavelength applications. Although tunable wavelength VCSEL array now is available, the swept wavelength of VCSEL by simply injection current becomes a

candidate for developing FBG interrogator. Additionally, due to shifting the Bragg wavelength not more than 10 nm and VCSEL array or MEMS VCSEL cost more than 100 times compared to VCSEL we used, our system offers an alternative a low-cost FBG interrogator. In this chapter, we also measure the wavelength-swept of VCSEL by injection current. We can sweep the wavelength of 1.4 nm with 2.45 mA modulation change. The important from this experiment, we obtained the relationship between the injection current and the wavelength, then we will use this relationship in the program we explain in Chapter 5.

Chapter 4: FMCW

4.1 Basic and principle of FMCW

Frequency Modulated Continuous Wave (FMCW) reflectometry was initially developed for radio detection and ranging (radar) technology. This technique has been established for six decades ago. Basically, this system transmits the FMCW signal to the target; a reflected signal, which reaches a target, is evaluated by comparing with the transmitted signal. Reflectometry based on frequency domain has some advantages than optical time domains such as resolution, sensitivity, measurement time, and signal to noise ratio (SNR). Fortunately, FMCW not only well-accepted in radar but also successfully applied in an optical system, which is called optical FMCW [67], [68]. The first paper regarding optical FMCW was reported by Brian Culshaw and P. Giles in 1982. Then, extensive researches on optical FMCW have been performed, so that some of them have already applied in practice [64].

Optical FMCW has several advantages over the classical optical interference as described in the following:

- a. Optical FMCW has the capability to measure the absolute distance
- b. Optical FMCW has higher accuracy and much longer measurement range
- c. Optical FMCW can be constructed in fiber optic so that more application can be performed
- d. Optical FMCW can be realized for multiplexed fiber optic interferometers.

In optical FMCW, waves come from an optical frequency that is continuously modulated. The angular frequency of FMCW $\omega(t)$ which transmits to laser source can be defined as:

$$\omega(t) = f_{\omega}(t) + \omega_0 \quad 45$$

where $f_{\omega}(t)$ is the optical angular frequency modulation, ω_0 is the central angular frequency. Due to reach a target, a reflected signal has a different path, which is

delayed by τ ($\tau = nl/c$). If the transmitted signal and reflected signal are combined, the intensity $I(t)$ will be:

$$I(t) = I_0\{1 + V\cos[F_\omega(t) - F_\omega(t - \tau) + \omega_0\tau]\} \quad 46$$

I_0 is the average intensity of the beat signal ($I_0 = I_1 + I_2$), V is a contrast of the beat signal, $F_\omega(t)$ is a primitive function of $f_\omega(t)$. Equation 46, is called the general equation of the optical FMCW interference [69].

In one part, optical FMCW is similar to heterodyne interference. In both interferences, the intensity of the resulting electric field depends on spatial and temporal coordinates. On the other hand, optical FMCW and heterodyne are different because the FMCW beat signal is more complex and more information than the heterodyne beat signal. Optical FMCW beat signal is related to delay time and optical path different [64], which means target information.

4.2 Analysis of FMCW Signal

The waveform used for modulating frequency of an optical wave can be operated various shapes. The modulated frequency in FMCW should be periodic function and easy to further processing. Three kinds of optical FMCW will be described as follow:

a. Sawtooth-wave optical FMCW

When a coherent light source is modulated by using a sawtooth waveform, a beat frequency resulted from the reference signal, and the reflected signal can be shown in figure 32. The solid curve represents the reference wave, and the dashed curve represents the reflected wave. Due to optical path different (OPD), interference between of them produces a beat signal, as shown in the dot-dashed curve. In the period $(-T_m/2, -T_m/2 + \tau)$, the beat frequency(v_b) is equal:

$$v_b = \frac{\Delta v v_m OPD}{c} \quad 47$$

where Δv is optical frequency modulation excursion ($\Delta v = \Delta\omega/2\pi$), v_m is frequency of modulation, OPD is an optical difference path. As shown in

figure 32, besides beat frequency, there is a doppler frequency $\overline{\nu}_D$ as expressed in equation 48:

$$\overline{\nu}_D = \frac{2n}{\lambda_0} S \quad 48$$

S is the speed of the moving object. Due to error from the doppler effect, sawtooth-wave FMCW is only suitable for static or slow-changing OPD.

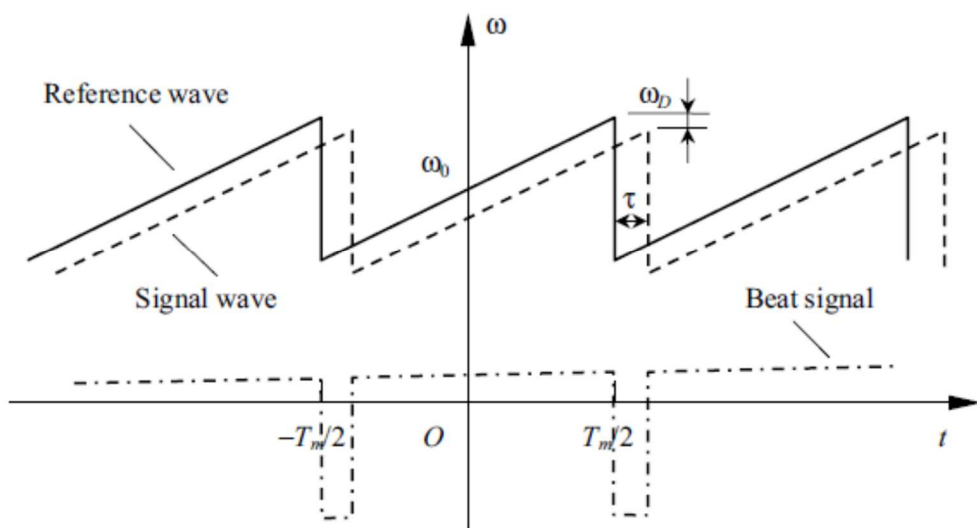


Figure 32. Sawtooth wave modulation FMCW [64].

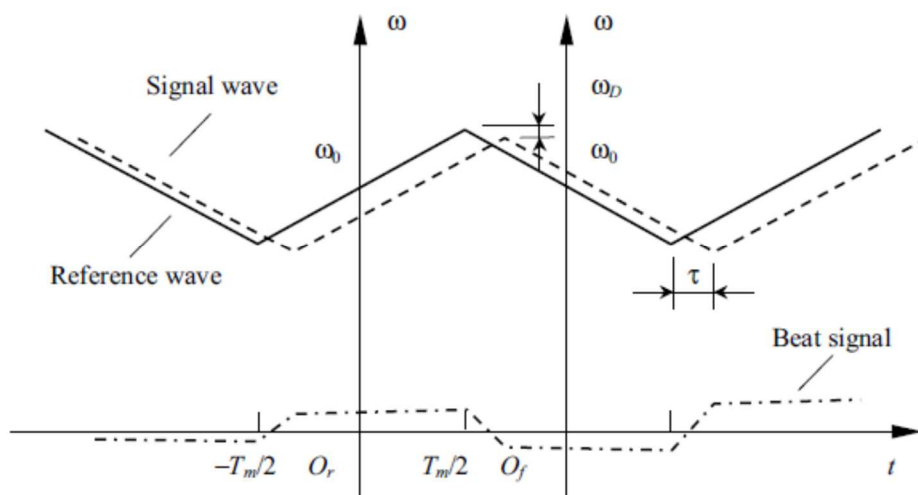


Figure 33. Triangular wave modulation FMCW analysis [64].

b. Triangular-wave optical FMCW

When the period of the triangular-wave modulation signal is $2T_m$, and for simplifying this period is divided into two parts, the rising and the falling period, as shown in figure 33. The Angular beat frequency for the rising period and falling period are:

$$\omega_{br} = \alpha\tau \quad 49$$

$$\omega_{br} = -\alpha\tau \quad 50$$

where α is the angular frequency modulation rate, the angular beat frequency for rising and falling periods is only different at signs operation. Triangular-wave optical FMCW also appears Doppler angular frequency shift same as sawtooth-wave FMCW. To define beat frequency, rising and falling period is usually divided separately. Triangular wave and sawtooth optical FMCW belong to linear FMCW. Both of them require a linear frequency modulation light source.

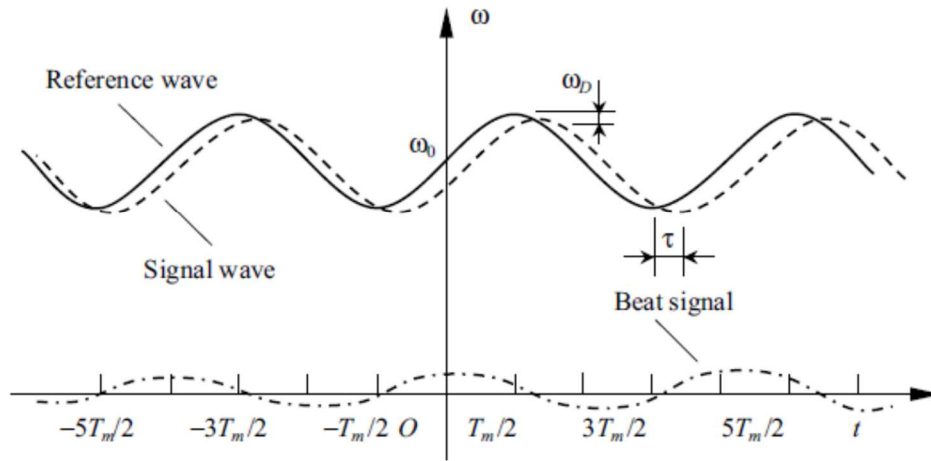


Figure 34. Triangular wave modulation FMCW [64].

c. Sinusoidal-wave optical FMCW

Figure 34 illustrates the sinusoidal-wave modulated signal of optical FMCW. The angular frequency of the beat signal is expressed in equation 51:

$$\omega_b = \frac{\Delta\omega\omega_m\tau}{2} \cos(\omega_m t)$$

51

As shown in equation 51, the angular frequency of the beat signal is not constant, and this shows the major weakness of sinusoidal-wave optical FMCW in practice [64], [70].

4.3 Incoherent FMCW

Optical FMCW is divided into two main kinds of systems, that is coherent FMCW (C-FMCW) and incoherent FMCW (I-FMCW). The significant difference between two systems is C-FMCW utilizes optical mixing, and I-FMCW employs electrical mixing [28]. Figure 35 shows the configuration of the I-FMCW optical ranging system. Basically, the I-FMCW optical ranging system is composed of an intensity-modulated laser source whose modulation frequency is linearly swept in time. The beat signal can be obtained by using the double-balanced mixer (DBM) and followed a low pass filter (LPF). The beat signal comes from the reflected light from the target and the modulation signal (reference signal). Figure 36 shows the instantaneous modulation frequency of the reflected and reference signals. The reflected signal is delayed by τ with respect to the reference signal due to the distance to the target, and the mixed-signal contains information a beat frequency corresponding to the distance to the target.

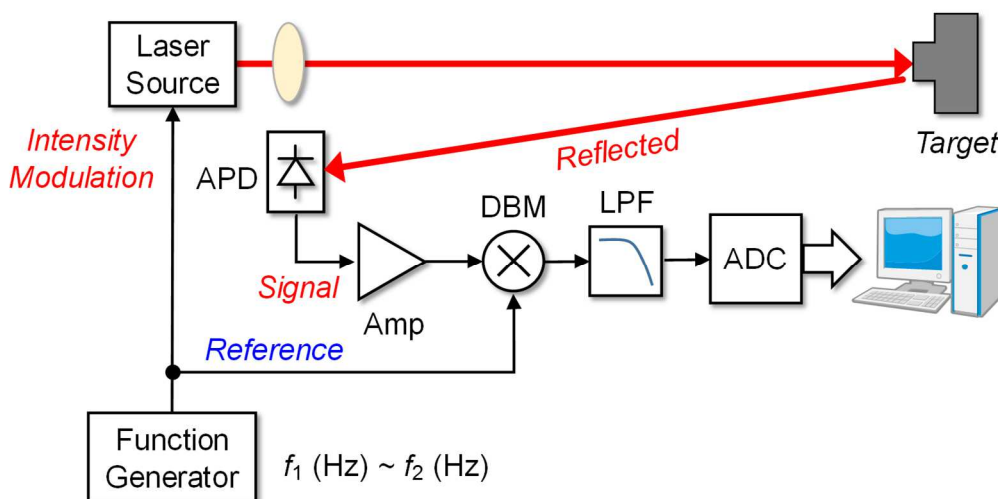


Figure 35. Configuration of the I-FMCW optical ranging system.

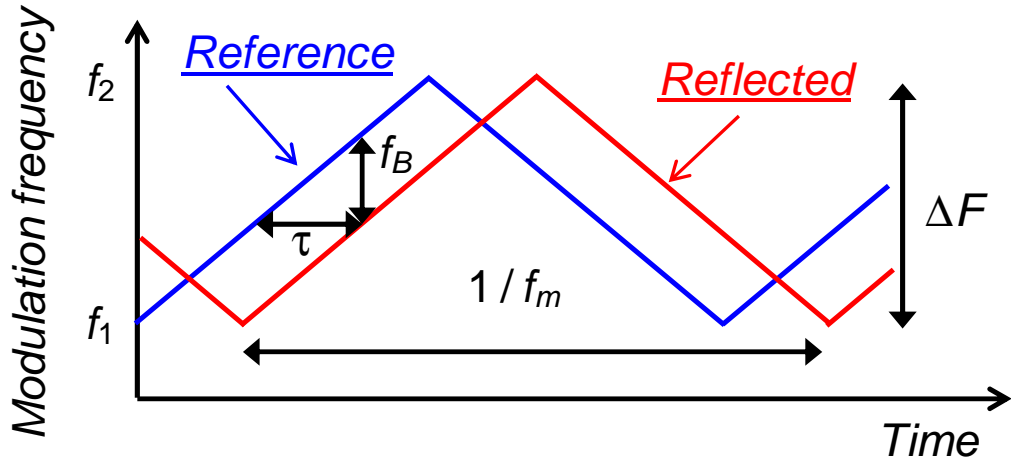


Figure 36. I-FMCW signal analysis.

The working principle of I-FMCW is described as following. The reflected signal detected by the PD $s(t)$, the reference signal $r(t)$, and the electrically mixed signal by the DBM $m(t)$ are expressed as:

$$r(t) = A \cos(2\pi f t) \quad 52$$

$$s(t) = B \cos\{2\pi(f - \gamma\tau)t\} \quad 53$$

$$m(t) = r(t) \times s(t) = \frac{AB}{2} [\cos\{2\pi(2f - \gamma\tau)t\} + \cos(2\pi\gamma\tau t)] \quad 54$$

$$f_b = \gamma\tau = 4nf_m\Delta F \cdot \frac{L}{c} \quad 55$$

where A and B are the magnitudes of the reference and the reflected signals, respectively, f is the instantaneous modulation frequency of the reference signal at a certain time, γ is the modulation frequency sweep rate in Hz/s unit, t is the time, τ is the delay time between the reflected and the reference signals, f_b is the beat frequency, f_m is the repetition frequency of the modulation frequency sweep, ΔF is the sweep range of the modulation frequency, L is the location of the FBG, n is the refractive index of optical fibers, and c is the speed of light in vacuum. The modulation frequency sweep rate γ is given as $\gamma = 2f_m\Delta F$ from figure 36, and the delay time τ is given as $\tau = 2nL/c$ considering the roundtrip propagation. As shown in the above equation, the mixed-signal $m(t)$ has the beat frequency f_b corresponding to the distance to the reflection point [71].

Another main parameter in I-FMCW is the spatial resolution, which is determined by the sweep range of the modulation frequency. The spatial resolution Δl_{FMCW} is given by the Rayleigh resolution as expressed in equation 56:

$$\Delta l_{FMCW} = \frac{c}{2n\Delta F} \quad 56$$

However, in FMCW analysis is usually involved a windowing that is used in the fast Fourier transform (FFT) for data processing; therefore, the beat spectrum is broadened. The spatial resolution was evaluated from the FWHM of the beat spectrum. The FWHM of the beat spectrum after multiplying a window to the I-FMCW ranging signal, Δl_{FWHM} , is given as [22]:

$$\Delta l_{FWHM} = 2 \times \Delta l_{FMCW} = \frac{c}{n\Delta F} \quad 57$$

In order to enhance the FWHM, it can be easily performed by increasing the sweep range of the modulation frequency ΔF by using a wideband sweep generator.

4.4 Fast Fourier transform (FFT) processing

Instead, in the time domain, the beat signal is simply to be understood if presented in the frequency domain. This task can be solved by spectrum analysis using fast Fourier transform (FFT) processing. The relation between the signal in the time domain and the frequency domain can be seen in equation 58:

$$X_f(f) = F\{x(t)\} = \int_{-\infty}^{\infty} x(t). e^{-j2\pi ft} dt \quad 58$$

where $X_f(f)$ is a complex signal in the frequency domain, $F\{x(t)\}$ is Fourier transform of $x(t)$, $x(t)$ is a signal in the time domain. According to Shannon's law of sampling, the sampling frequency (f_s) must be at least twice the bandwidth of the input signal (B_{in}). In a discrete Fourier transform, the calculated spectrum is made up of individual components at the frequency bin, as expressed in equation 59 [72]:

$$f(k) = k \cdot \frac{f_s}{N} = k \cdot \frac{1}{NT_s} \quad 59$$

where $f(k)$ is discrete frequency bin, k is an index of discrete frequency bins (0, 1, 2...), T_s is sampling period, and N is the length of discrete Fourier transform. Due to Nyquist criteria, and recall equation 55, the sampling rate (f_s) for maximum length (L_m) should be:

$$\begin{aligned} f_s &= 2f_b \\ f_s &= 2.4nf_m\Delta F \cdot \frac{L_m}{c} \\ f_s &= 8nf_m\Delta F \cdot \frac{L_m}{c} \end{aligned} \quad 60$$

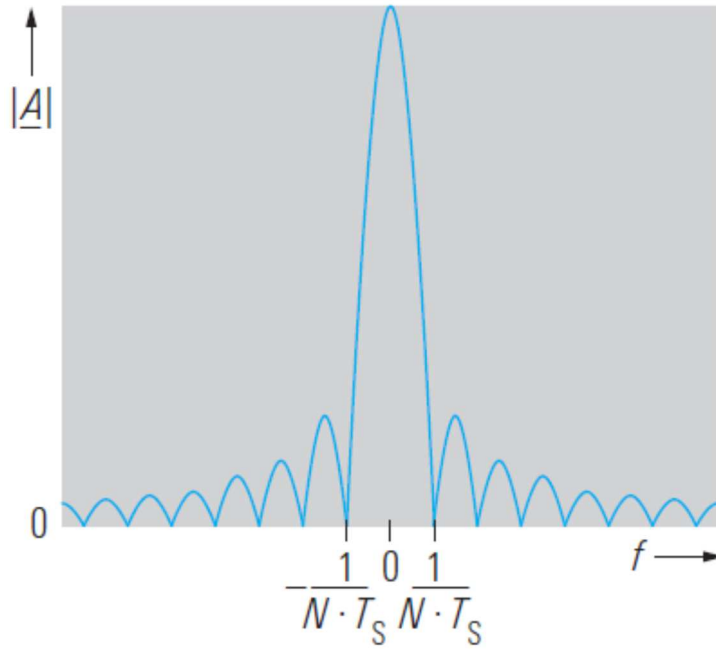


Figure 37. FFT signal with main lobe and sidelobe [72].

In FFT processing, the response signal reveals a main lobe and sidelobes, as shown in figure 37. The width main lobe represents the signal resolution, and the sidelobe indicates the strong sinusoidal signal can overpower the main lobe response of a nearby weak sinusoidal signal. The peak of the main lobe and reducing the sidelobes can be governed by selecting a window function; for example, by using the Hanning window can be reduced a sidelobe until 60 dB [73].

4.5 Summary

Optical FMCW provides better spatial resolution and higher sensitivity than optical reflectometry based on time division. For long-range measurement, due to coherent FMCW requires a light source with narrow linewidth, incoherent FMCW may offer a solution for low-cost and long-range measurement because of incoherent FMCW involve electronic mixing for combining reflected signal and the reference signal. Among the frequency modulation that modulates optical light in our system, we will use the triangular waveform. Even though the beat signal can be found from the increasing section and decreasing section, we will decide only increasing section to find a beat signal.

Chapter 5: Development of FBG Interrogator System

5.1 Set up of FBG interrogator

To realize FBG Interrogator for long-range SHMS and multi-point FBG sensors, we combine VCSEL and I-FMCW optical ranging system. The setup of our system is illustrated in figure 38. A single-mode VCSEL (RC32xxx1-FFP from RayCan) emitting at 1560 nm is employed as a laser source. The temperature of the VCSEL is controlled to 20°C by Thermo Electro Controller (TEC) provided by pigtailed laser diode mount (LDM9LP from Thorlabs). The VCSEL is sinusoidally intensity-modulated by the injection current modulation, and the modulation frequency is linearly swept in time from 10 MHz to 160 MHz with 50 Hz repetition frequency by the signal generator (SG: DG4162 from RIGOL) through RF modulation pin provided laser mount LDM9LP. The emitted light from the VCSEL is amplified up to 6 dBm by using the erbium-doped optical fiber amplifier (EDFA LXI 2000 from LUXPERT) and is then launched into single-mode fibers connecting with three FBGs (FBG1, FBG2, and FBG3) fabricated by Tatsuta through the circulator. The specification of FBG1, FBG2, and FBG3 are shown in table 1.

The reflected light from the FBGs is detected with the photodetector (PD PDA10CF-EC from Thorlabs). The wavelength of the VCSEL is controlled by the injection current to measure the reflection spectrum of the FBGs through a laser driver (LD ITC 502 laser Combi controller from Thorlabs). To confirm the possibility of remote sensing, we insert optical fibers, FO1, FO2, and FO3 between FBGs. The lengths of FO1 and FO2 are 1000 m and 5640 m, respectively, and the length of FO3 is selected from 40 m, 10 m, and 5 m. The ranging signal is generated by electrical mixing of the reflected signal and the reference signal by using the double-balanced mixer (DBM Mixer ZAD-1-1 from Mini-Circuits) followed by the low pass filter (LPF), and then the ranging signal is sampled using the high-speed data acquisition (DAQ) board (MC USB-2020 from Measurement Computing). The data acquisition board has two analog input channels with the sampling rate until 20 MS/s and a 12-bit resolution and synchronization channel. For measurement purposes, analog input 0 (AI.0)

acquires ranging signal, and analog input 1 (AI.1) acquires ILDSignal from laser driver. Due to the modulation frequency sweep is bidirectional with 10 ms of the frequency increasing section and 10 ms of the frequency decreasing section, we acquire a ranging signal only the frequency increasing section. To ensure starting data acquisition only from the beginning of the frequency section, a synchronization channel from the DAQ board is connected to the signal generator by using a transistor-transistor logic (TTL) signal, which is generated according to increasing and decreasing section. Then, In order to sweep the wavelength of the VCSEL, the injection current of the VCSEL is changed in stepwise [21] by using the programmable voltage source (8532 Digital Electrometer from ADCMT).

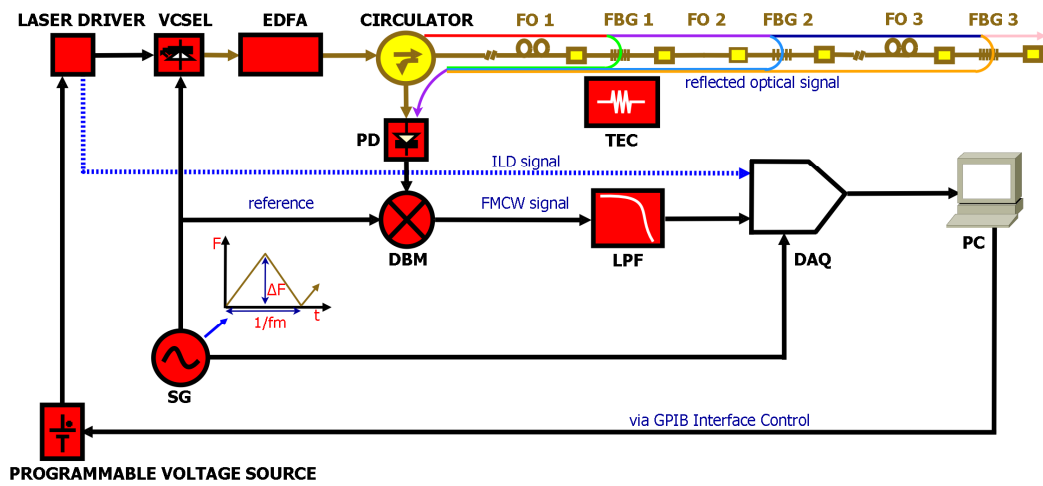


Figure 38. Configuration of the proposed system for FBG interrogator.

Table 1. Specification of FBG1, FBG2, and FBG3.

	Bragg wavelength (nm)	Reflectivity (%)	Bandwidth (nm)
FBG1	1560.01	5.59	0.083
FBG2	1560.04	5.81	0.110
FBG3	1560.03	6.24	0.095

5.2 Development a software

All systems shown in figure 38 is controlled with a program using LabVIEW (from National Instruments). However, VCSEL and signal generator

operate continuously. We made an algorithm of our program as following the flowchart shown in figure 39. Data communication from DAQ MC2020 to the personal computer (PC) by using a USB Interface and from programmable voltage source by using general-purpose interface bus (GPIB) interface control. In order to get data in frequency increasing section only from the signal generator, we set a rising edge from the TTL signal to trigger data acquisition of ranging signal. Some Parameters (V_{init} , V_{step} , and V_{final}) for setting programmable voltage sources are defined to modulate injection current of VCSEL through laser driver. We set the current (I_{DC}) of VCSEL at 5.21 mA. Because we modulate by a voltage source, injection current of VCSEL change from 5.21 mA to 6.85 mA when increasing current, and from 6.85 mA to 5.21 mA for decreasing current continuously. In our measurement, we process for FBG interrogation only increasing the current section. The obtained relationship between the injection current and the wavelength from figure 31 in Chapter 3 is stored in our program to define the wavelength of VCSEL.

The fast Fourier transform (FFT) with Hanning Window is carried out to obtain the beat spectrum in order to determine the position of the FBGs by using equation 55. The user can select the number of samples and sizes of FFT. In order to improve spatial resolution, we applied zero paddings after the Hanning window with automatically provided from the difference between a number of samples and sizes of FFT. In addition, we also apply to skip a number of samples at the beginning and last acquisition. By applying a peak searching as expressed at equation 22 in Chapter 2, we define the Bragg wavelength of each FBG. The system can also recognize where and which FBG is being read by ranging signal produced by I-FMCW in meter or frequency domain in Hz. Lastly, the program also provides some features such as plotting and storing data.

Figure 40 shows a graphical user interface (GUI) of the program FBG interrogator based on the I-FMCW ranging system, which is developed by LabVIEW. In our experiment, we set the sampling rate of DAQ 2 MHz, the number of samples of 20,000, numbers of skip 4000, and FFT sizes 65,536. We also apply ten times for running averaging by the root mean square (RMS) averaging to determine the beat spectrum. The left graph shows 3 reflection

signals of FBGs, which means our system clearly identifies three FBGs, and in the right graph shows the result of Bragg wavelength from three FBGs during measurement in time.

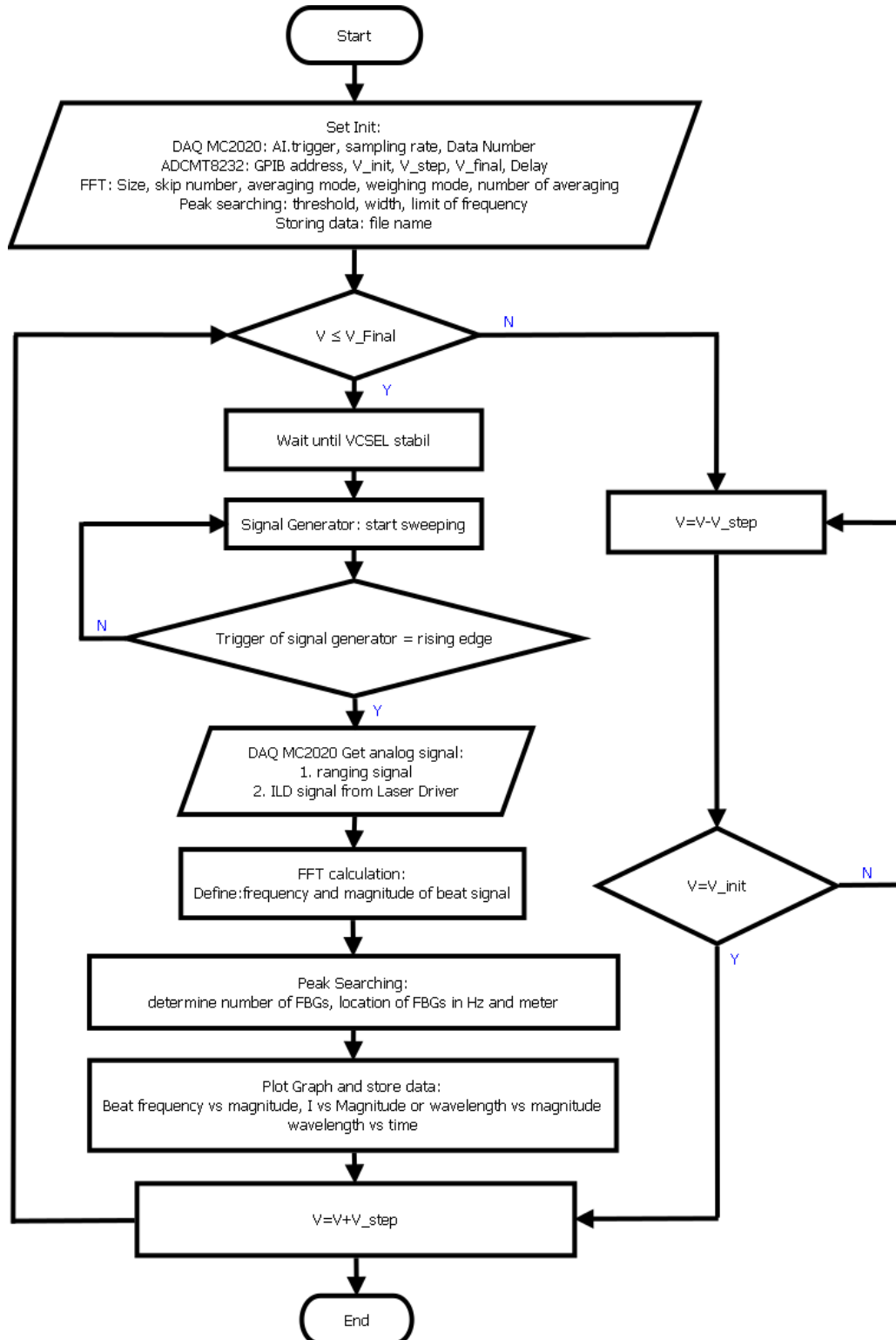


Figure 39. Flowchart of LabVIEW program for the proposed system.

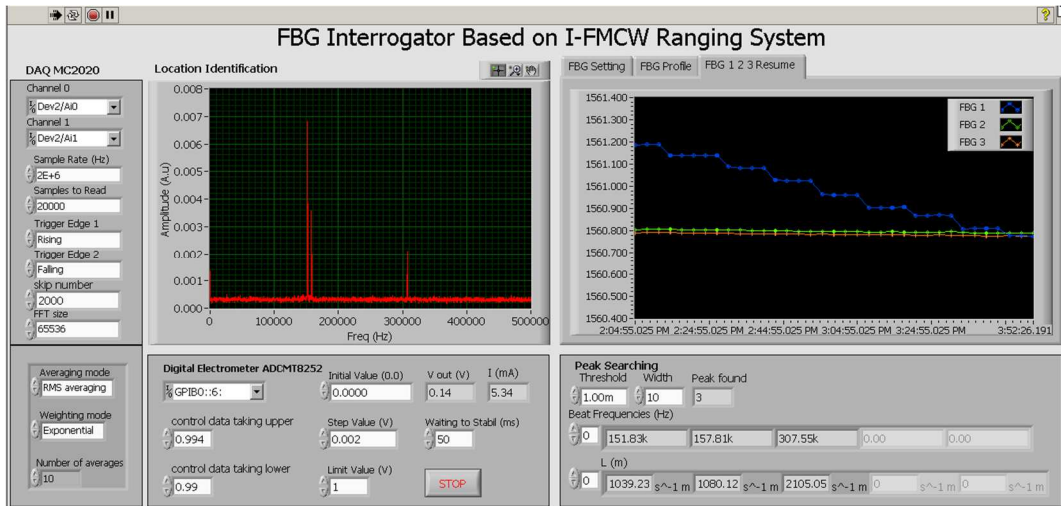


Figure 40. GUI of the FBG interrogator based on I-FMCW.

5.3 Frequency response

In order to mitigate optical and electrical frequency dependency, we first observe the frequency response of our system by using a network analyzer. The frequency response is shown in figure 41. The modulation bandwidth of the VCSEL including the VCSEL mount, is 500 MHz, and the 3 dB bandwidth of the PD (including the following amplifier) is 150 MHz. The group delay from the VCSEL to the PD is constant up to 500 MHz, as shown in figure 42. Although the 3 dB bandwidth of the PD is slightly narrower than the maximum modulation frequency, no compensation of the frequency response was needed and applied.

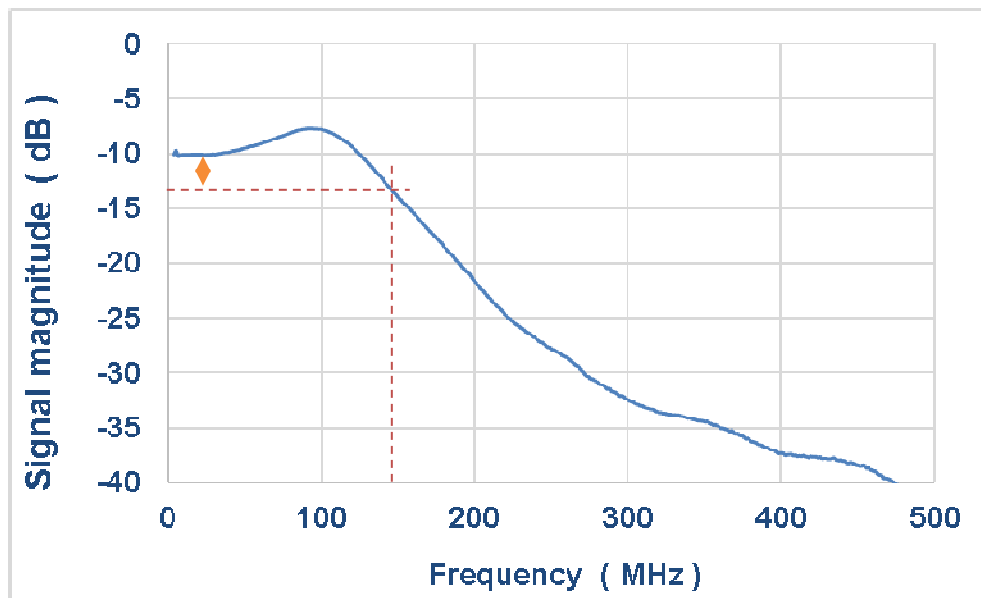


Figure 41. Frequency response of the proposed system.

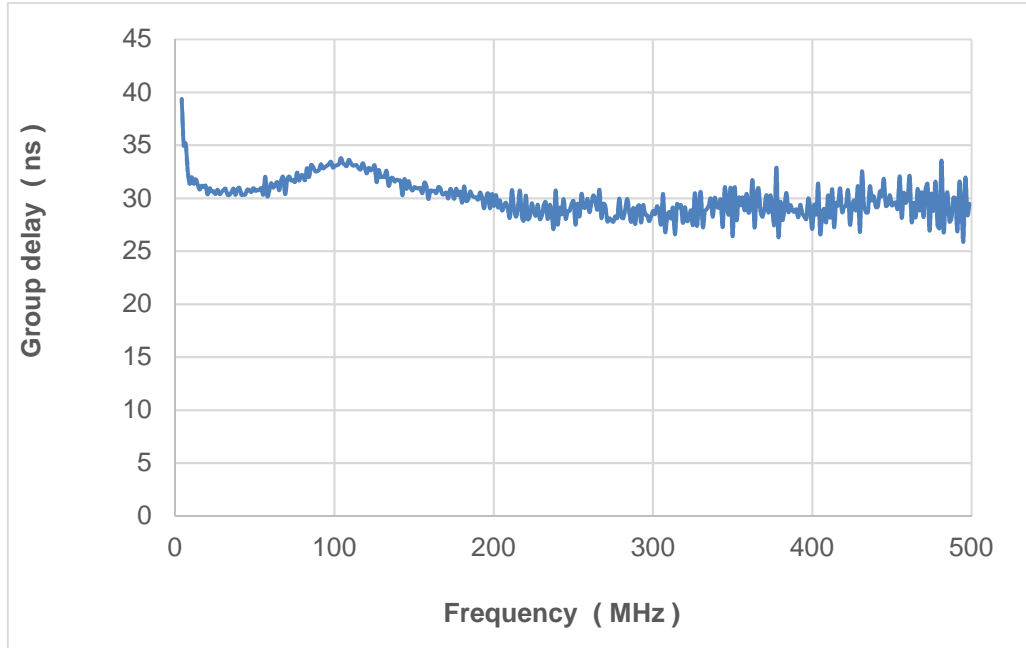


Figure 42. Group delay of the proposed system.

5.4 Summary

We developed hardware equipped by software to interrogate multi-point FBGs by combination VCSEL and I-FMCW optical ranging. The system has been successfully showed the reflection spectrum of three FBGs and determined Bragg wavelength. Then, we demonstrate the performance of our proposed system, including long-distance, temperature, and strain. For temperature measurements, the ambient temperature of FBG1 will be changed in the range of 25°C ~ 45°C by using a TEC. For strain measurements, we will vary strain from 369 μm to 2137 μm of FBG3 using the cantilever beam method. We then show and analyze the performance of multipoint capabilities, the spatial resolution, the spectrum response, and long-term stability.

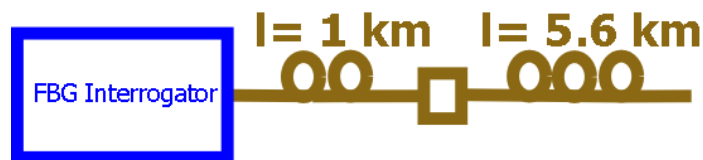
Chapter 6: Long-range and spatial resolution measurement

6.1 Measurement of long-range optical fiber

The main aim of the development of FBG interrogator in our dissertation is to be applied in structures monitoring. Due to structures are usually very large or very long area, FBG interrogator in these applications should be capable of measuring a large or very long area. To confirm long-range measurement, we test our system to measure very long optical fiber without FBGs. To do this, we measure the beat spectrum from Fresnel reflections at the output facets of a 1000 m-long and a 6640 m-long optical fibers as illustrated in figure 43. For a 6640 m-length configuration, we connect 1000 m of optical fiber in figure 43(a) with a 5640 m-long optical fiber.



(a)



(b)

Figure 43. Illustration of long-range measurement for length of the optical fiber; (a). 1000 m and (b) 6640 m.

The result of the measurement of long-range measurement is shown in figure 44. The horizontal axis in figure 44 represents the length of the optical fiber in kilometer (km), which is automatically calculated by using a program based on equation 55. The vertical axis in figure 44 represents the magnitude of the reflected beat signal in a logarithmic scale, a decibel (dB). The Fresnel reflection peak for the 1000 m-long optical fiber and 6640 m-long optical fiber are clearly

found in figure 44. The Peak of Fresnel reflection of 1000 m-long optical fiber is found at 1.041 km with a signal to noise ratio (SNR) of 45 dB. The peak of Fresnel reflection of 6640 m-long optical fiber is also found at 6.68 km with an SNR of 27 dB. The SNR of the 6640 m-long optical fiber is weaker than the Fresnel reflection peak for the 1000 m-long optical fiber due to the attenuation of the optical fiber. Nevertheless, our system might be a possibility for long-range and large SHMS.

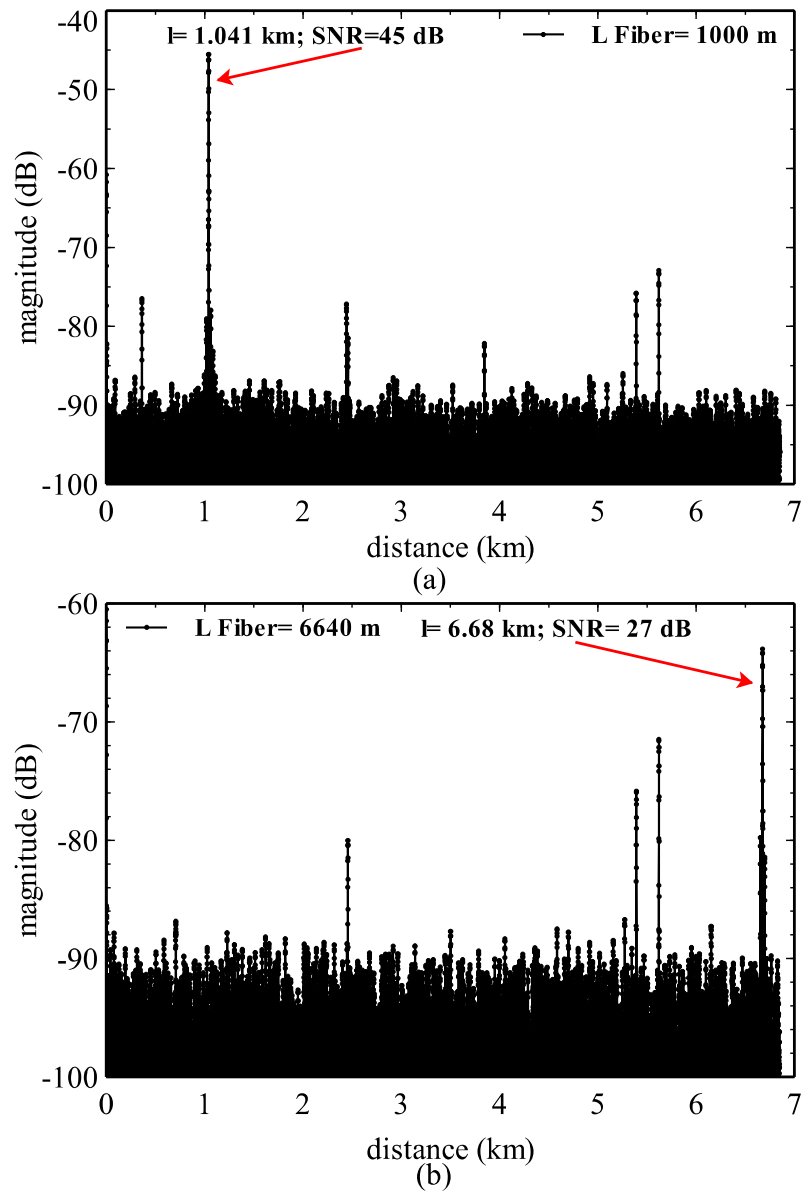


Figure 44. Measured beat spectrum of Fresnel reflection of an optical fiber with length of (a) 1000 m and (b) 6640 m.

After successfully tested our system to measure long-range optical fiber, we then install three FBGs into our system over 6.6 km in length, as illustrated in figure 45. The lengths of FO1 and FO2 are 1000 m and 5640 m, respectively, in order to validate the capability of long-range FBG sensing, and the length of FO3 is short optical fibers between three optional lengths (40 m, 5 m, or 3 m) to confirm the spatial resolution and also identify the exact location of FBG installed. In this measurement, all of FBGs are kept in room temperature (23°C) and unstrained condition.

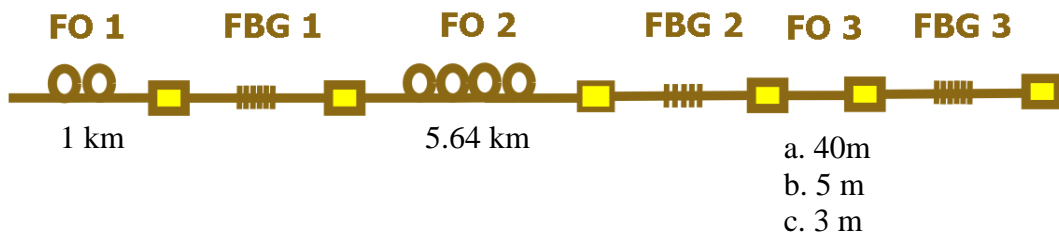


Figure 45. Illustration of long-range measurement with three FBGs.

The measured beat spectrum of each FBG is shown in figure 46. Due to FBG2 and FBG3 are separated by short optical fiber, those FBGs seem only one spectrum. Hence, we zoom those spectra and insert them into the main graph. Therefore, we can clearly observe three reflection peaks from FBG1, FBG2, and FBG3 when the short of an optical fiber of FO3 is 40 m-long for figure 46(a), 5 m for figure 46(b), and 3 m for figure 46(c). These results indicate that our system can identify where FBGs are installed.

6.2 Spatial resolution measurement

Figure 46 also shows the capability of our system to distinguish between two nearest FBG signals by using spatial resolution. Two FBG spectra still can be clearly separated when the length of FO3 of 3 m as shown in figure 46(c) because the full-width at half maximum (FWHM) is 1.5 m in our system as shown in figure 47. This result suggests that the distance between two nearest FBGs on the SHMS based on I-FMCW in our system should be more than 1.5 m. Nevertheless, the distance between FBG about 1 m is sufficient for monitoring most civil structures [74].

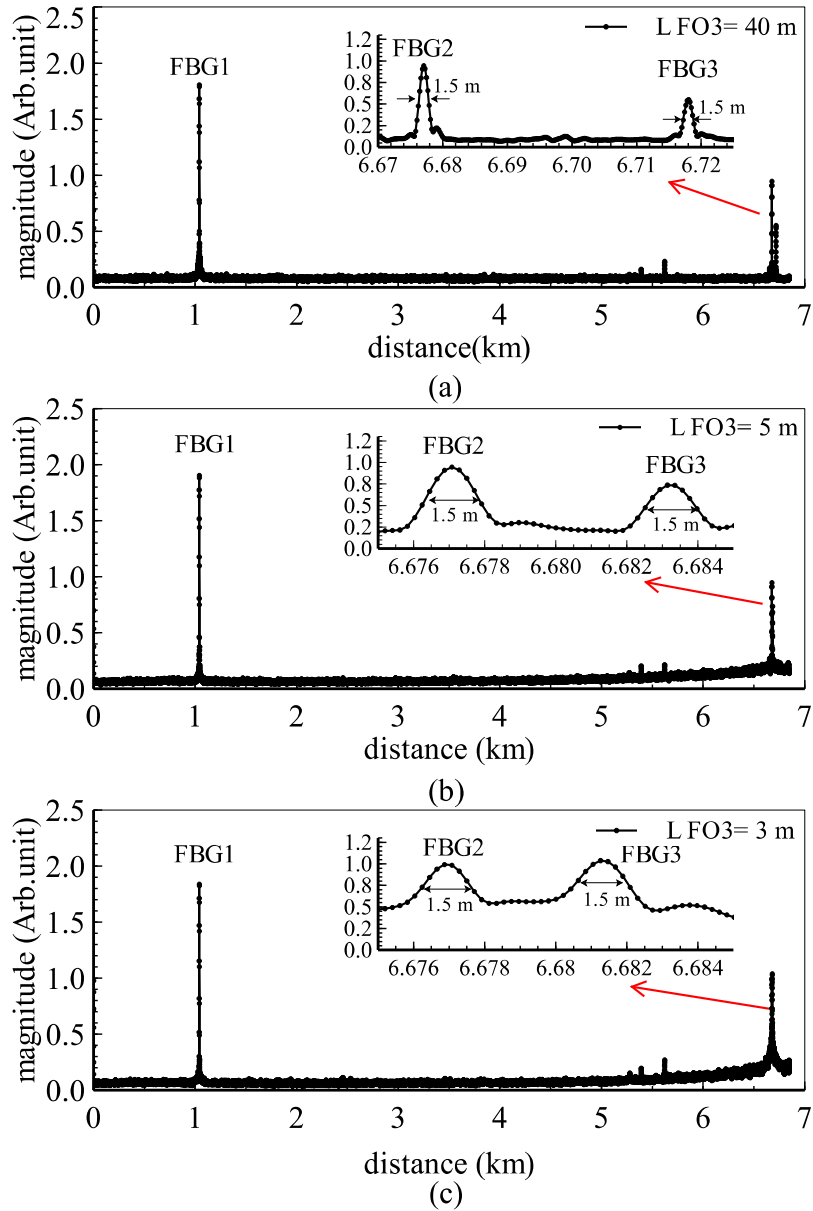


Figure 46. Measured beat spectrum for different FO3 length, (a) 40 m, (b) 5 m, (c) 3 m at the same temperature, and unstrained.

We discuss the spatial resolution of the I-FMCW spectrum again. Theoretically, the spatial resolution is determined by the sweep range of the modulation frequency, as expressed in equation 56. In our study, $\Delta F = 150$ MHz, and then $\Delta l_{\text{FMCW}} = 69$ cm for $n = 1.45$. Due to our program using a Hanning window in the FFT, The spatial resolution is evaluated from the FWHM of the beat spectrum is given by equation 57 is $\Delta l_{\text{FWHM}} = 1.38$ m in this study. Since the experimental FWHM has shown in figure 47 is 1.5 m almost same as the

theoretical FWHM. However, we can easily enhance the FWHM by increasing the sweep range of the modulation frequency ΔF by using a wideband sweep generator.

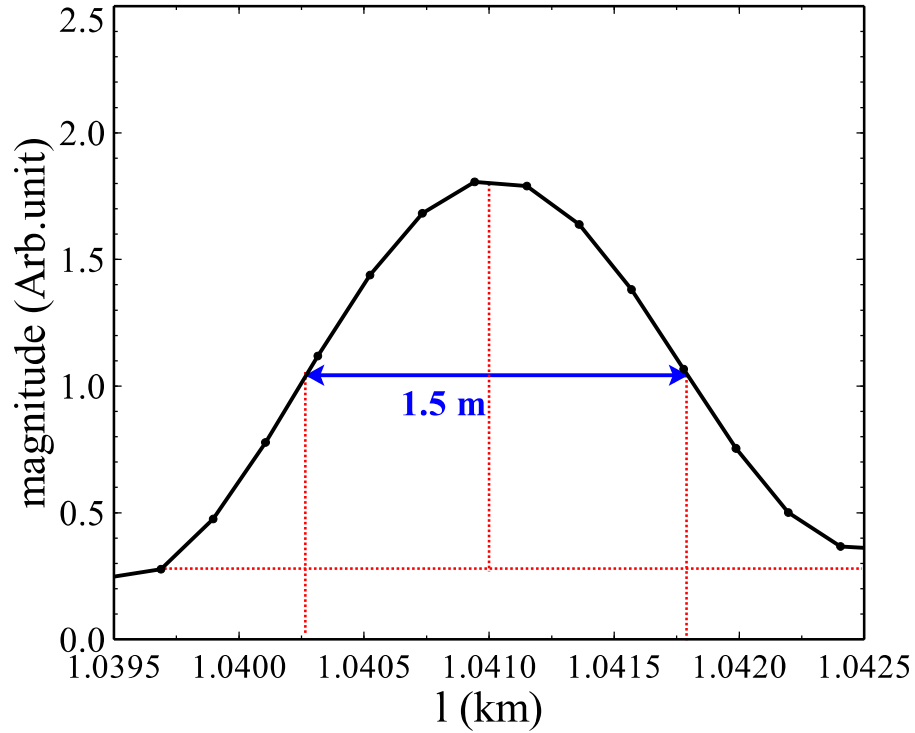


Figure 47. The spatial resolution of reflection of FBG.

Table 2. FBGs location identification.

Figure	Location of FBG1 (km)	Location of FBG2 (km)	Location of FBG3 (km)
7(a)	1.0410	6.6771	6.7181
7(b)	1.0410	6.6771	6.6831
7(c)	1.0410	6.6771	6.6813

6.3 Identification of sensor location

In the SHMS, precise location identification for large and long measurement ranges is required in order to early for evaluating the structures. To do this, we observe the precise location of the FBGS sensor. The measured

locations of FBGs are shown in table 2, which is tabulated from figure 46. The measured locations of the FBGs are almost the same if we compare to the installed position of FBG1, FBG2, and FBG3 which are connected by FO1, FO2, and FO3 as shown in figure 45.

6.4 Summary

According to the results of the measurement, our system has the capability to explore a multi-point FBGs sensor with an area over 6.6 km. Although three FBGs sensors have Bragg wavelength almost same, each FBG can be clearly distinguished by each location where FBG installed. This situation is difficult when captured by using OSA. The smallest distance between two nearest FBGs can be installed in this system is 1.5 m. However, we can enhance by increasing the frequency sweep of the signal generator and the bandwidth of photodetector. Our system also provides information about the precise location of the FBG sensor. This enables to help of a stakeholder for taking action when one or more FBG sensors when giving a signal of critical information regarding the health of structures.

Chapter 7: Temperature Measurement

7.1 Temperature FBG identification by scanning wavelength

In Chapter 6, we have demonstrated that the FBG interrogator developed by our system to identify the reflected signal from FBGs and also to define their locations. We then test our system to measure temperature by using a configuration of the length of optical fibers, as illustrated in figure 48. The ambient temperature of FBG1 is set by TEC at 40°C, but FBG2 and FBG3 are still kept at room temperature. The injection current of the VCSEL is changed automatically by the program from 5.21 mA to 6.85 mA with 3.28 μ A step, corresponding to the wavelength change from 1560.27 nm to 1561.20 nm with 1.87 pm step. We set 50 ms for delay time after the injection current change in order to achieve the stable wavelength of the VCSEL. Totally the measurement time is 90 ms to scan temperature FBG from room temperature to 40 °C.

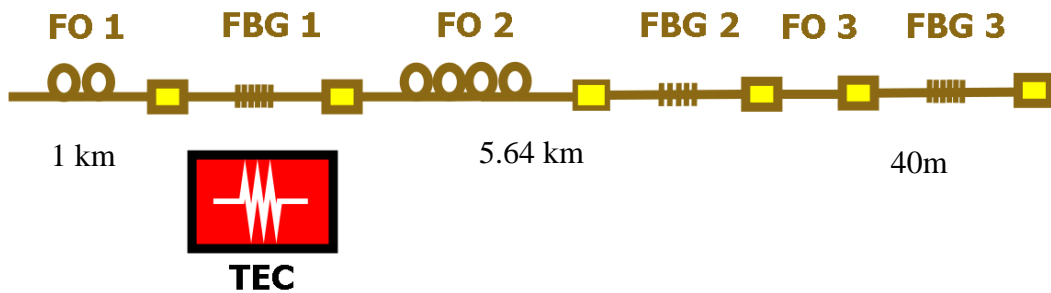


Figure 48. Illustration of temperature measurement by using the proposed system.

The measured results to the reflected signal of FBGs when setting at room temperature and 40 °C are shown in figure 49(a) and (b). The horizontal axis represents the distance of FBGs in km, and the vertical axis is the magnitude of beat signals in arb.unit (A.u). In figure 49(a), we find two peaks reflected signals for FBG2 and FBG3 when the VCSEL was tuned wavelength at 1560.740 nm. Since the ambient temperature of FBG3 was set at 40°C, there was no signal when the wavelength of VCSEL at 1560.740 nm. If we compare to figure 50, the VCSEL was tuned almost same, that was 1560.744, we find three of beat signals because in this figure all of FBGs were set at room temperature and unstrained. Thus, wavelength 1560.740 nm corresponds to the Bragg wavelength of the FBG

around room temperature. On the other hand, when the wavelength of VCSEL was tuned at 1560.955 nm, we find only one peak of FBG1 as shown in figure 49(b). Because the temperature of FBG1 was 40°C, the wavelength at 1560.955 nm corresponds to the Bragg wavelength at approximately 40°C.

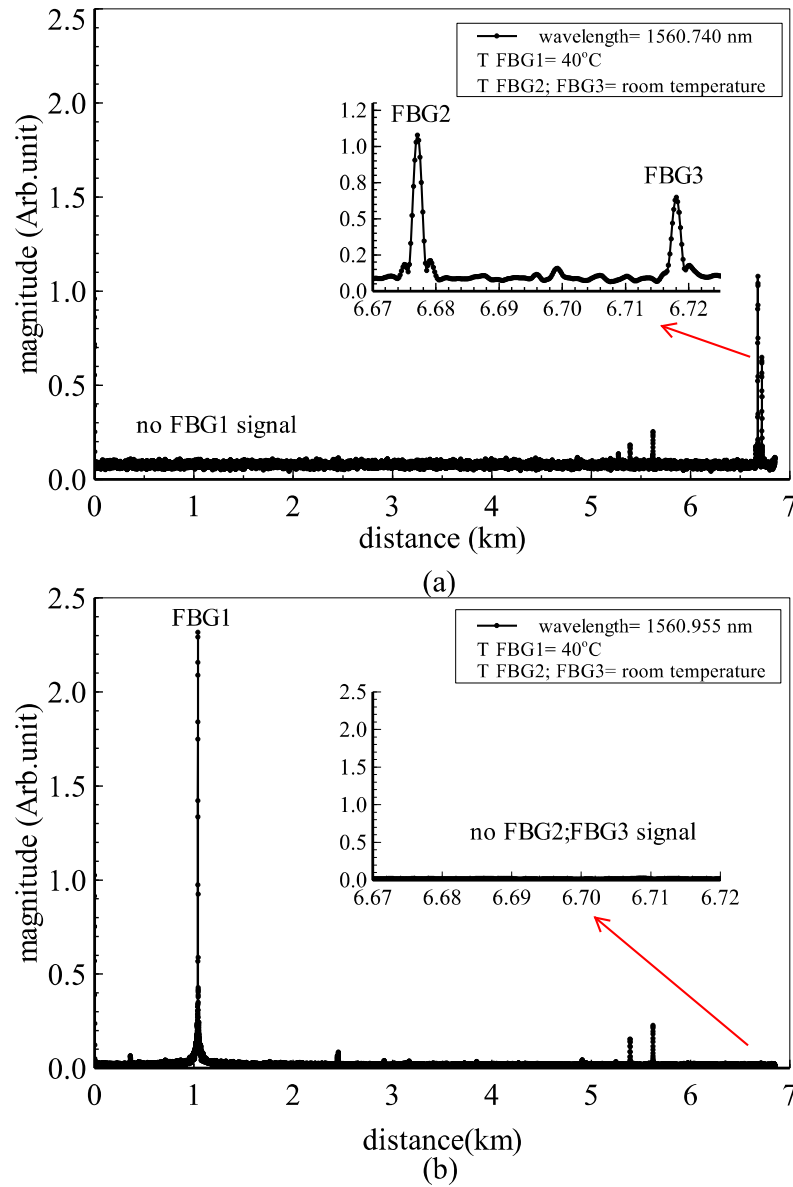


Figure 49. Measured beat spectrum for wavelength of (a) 1560.740 nm and (b) 1560.955 nm when the temperature of the FBG1 is 40°C, and the temperature of the FBG2 and FBG3 are room temperature (approximately 23°C).

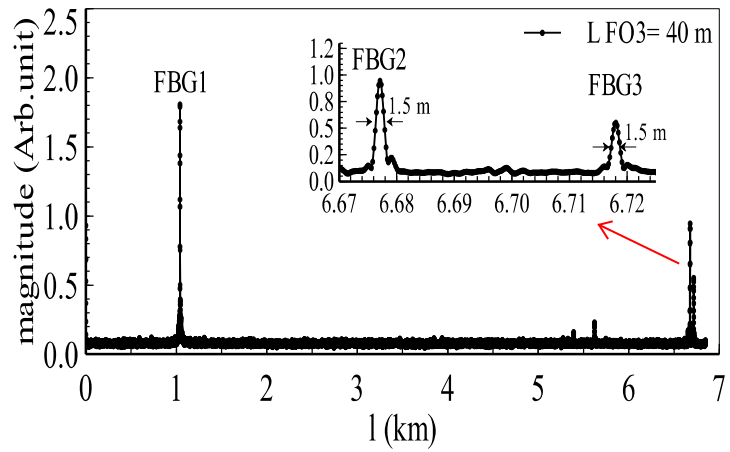


Figure 50. Measured beat spectrum for wavelength of 1560.774 nm when temperature of all FBGs at room temperature.

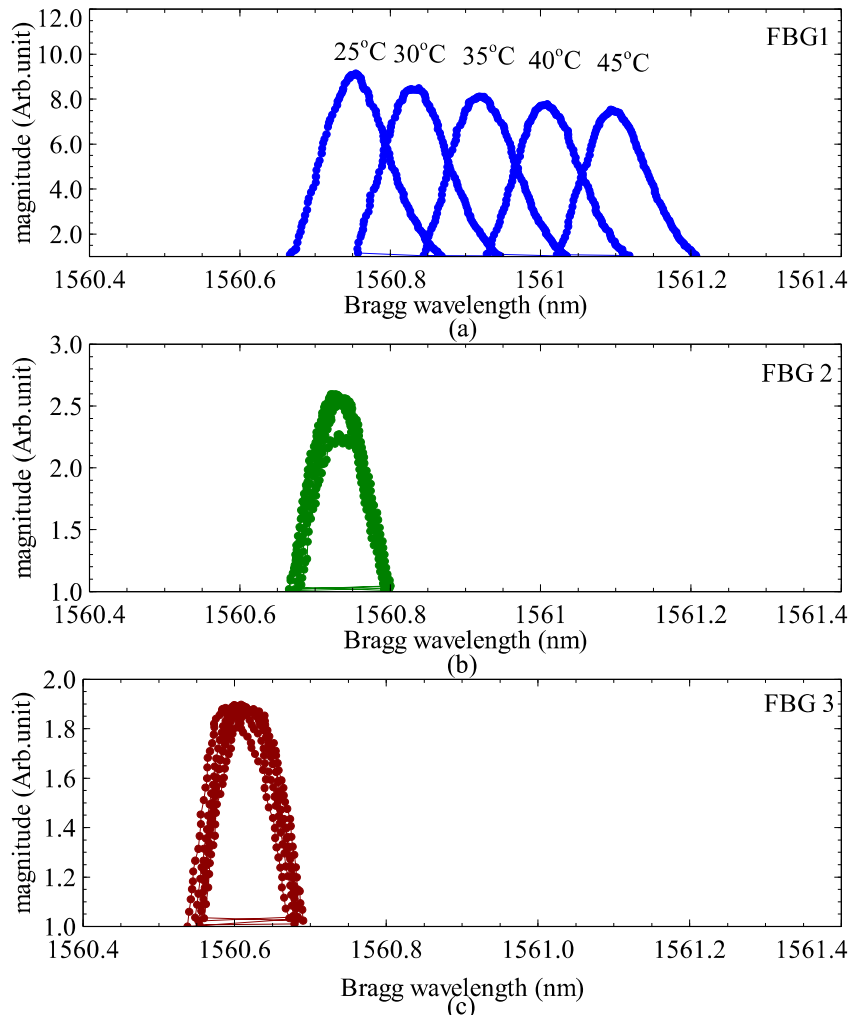


Figure 51. Spectrum of (a) FBG1, (b) FBG2, and (c) FBG3 when the temperature of FBG1 is changed.

7.2 Spectrum Profile of FBG when temperature change

We then measure the Bragg wavelength shift of the FBGs against the temperature change to evaluate the temperature sensitivity. In this experiment, the ambient temperature of FBG1 was increased from 25°C to 45°C in 5°C step, and contrary the temperature of FBG2 and FGB3 are kept at room temperature. The reflection spectra of all FBGs are shown in figure 51. The horizontal axis represents the wavelength of VCSEL in nm, and the vertical axis represents the magnitude of spectra in A.u. We find the reflection spectrum of FBG1 in figure 51(a) is shifted to longer wavelength according to the temperature increase, while the reflection spectra of FBG2 and FBG3 in figure 51(b) and (c), respectively, are unchanged. During the experiment, the room temperature is almost constant, therefore the temperature of FBG2 and FBG3 are also unchanged.

7.3 Transfer function of FBG temperature sensor

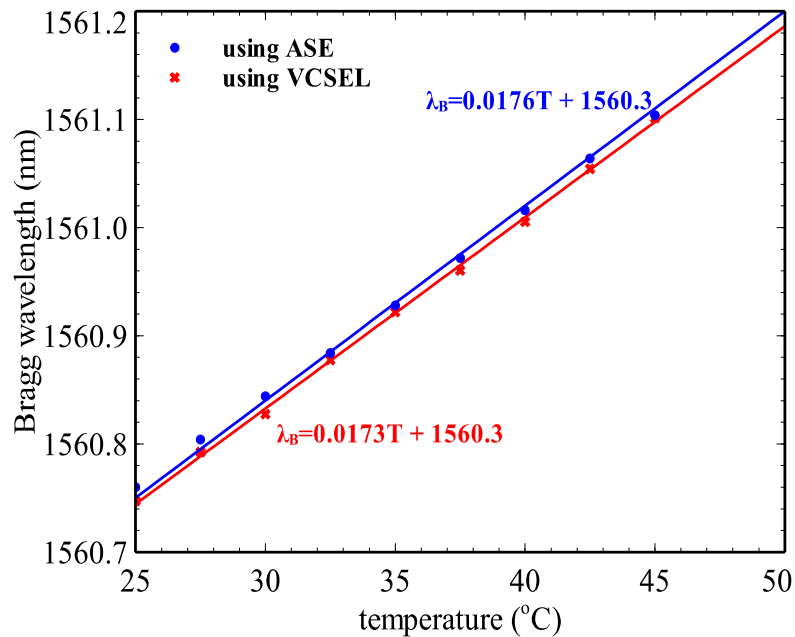


Figure 52. Transfer function of temperature FBG sensor.

Next, we examine only the response of FBG1 when the ambient temperature increase from 25°C to 45°C in 2.5 steps. Figure 52 shows the correlation between the temperature of FBG and the Bragg wavelength of FBG1. Bragg wavelength is automatically calculated by equation 22. The Bragg

wavelength of FBG1 is linearly increased with the temperature as expressed in equation 11 and match with the reported article by Song et al. [75]. The expression shown in figure 52 also gives the temperature sensitivity of FBG1 is $17.3 \text{ pm}/^\circ\text{C}$ and is almost the same as a typical FBG, which is reported by other researchers, that is between $11 \text{ pm}/^\circ\text{C} \sim 14 \text{ pm}/^\circ\text{C}$ [32], [35], [36].

In order to validate the result of FBG temperature measurement by using our system, we compare it with another method. We also measured the Bragg wavelength shift against the temperature change by using an OSA and an amplified spontaneous emission (ASE) as a broadband light source, as mentioned in figure 19 Chapter 2. The result is now also shown in same figure 52. The blue line expresses the result of temperature FBG measurement by using ASE and OSA, and the red line shows result measurement by using our system. Both results show almost the same trends and correlations.

7.4 Long term stability testing

Besides location and physical parameters, a critical factor in practical SHMS is long-term stability. This factor is important because FBG interrogator for SHMS will be applied to monitor structures every time and long term. This experiment was carried out for 23 hours from 11.30 pm until 10.30 pm the next day. The ambient temperature of FBG1 was kept in 40°C , and FBG2 and FBG3 were kept at room temperature. The result measurement can be found in figure 53. The horizontal axis is a time period in an hour, and the vertical axis represents the Bragg wavelength each FBGs. Figure 53 shows the Bragg wavelength of FBG1 is almost stable at 1561.0 nm which corresponds to 40°C , and the Bragg wavelengths of FBG2 and FBG3 are 1560.7 nm and 1560.6 nm . However, around 15 hours from the initial test (with a circle marked in figure 53), the Bragg wavelengths of all the FBGs are slightly decreased for a short time and then turned to stable because in this situation, our laboratory was opened for several minutes. During 23 hours, the temperature of FBG1, FBG2, and FBG3 is slightly changed at this time. To evaluate stability, we calculated error by using root mean square error (RMSE) as expressed in equation 61:

$$RMSE = \sqrt{\frac{(T_m - \bar{T})^2}{N}}$$

61

where T_m is the measured temperature of FBG, \bar{T} is average measured temperature, and N is number of measurements. Error for the FBG1 is as low as 0.6°C. This result shows that the system is well stable for long-term operation. The RMSE of FBG2 and FBG3 are 0.6°C, and 0.7°C, respectively. This means the room temperature is also constant for 23 hours.

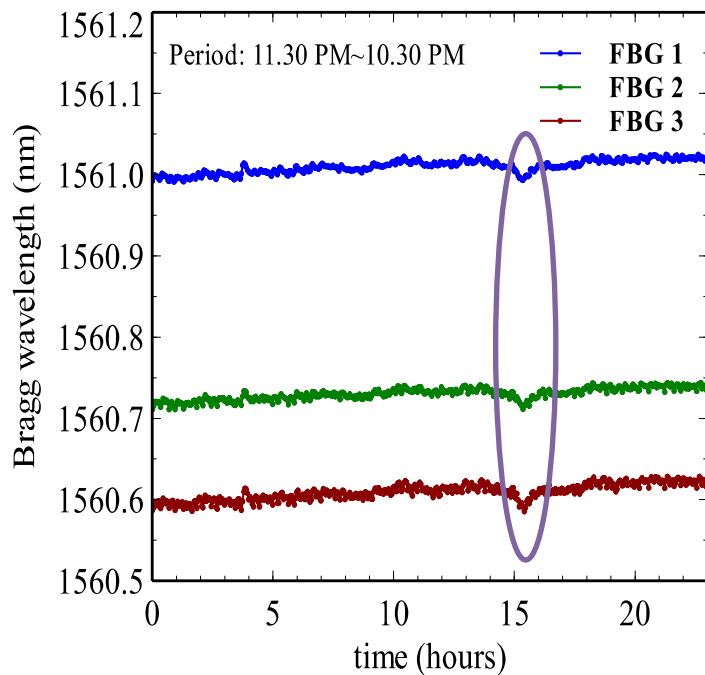


Figure 53. Stability and reliability testing of the proposed system for 23 hours.

7.5 Summary

The FBG interrogator, which is developed with our proposed method, has been successfully measured the temperature by using multipoint FBG sensors. Our system recognized the temperature by Bragg wavelength, which is reflected from each FBG. The spectrum of Bragg wavelength shifts to longer temperature changes. By this setting, we can measure temperature from 25°C to 45°C. However, our system possible to measure temperature more than this range (25°C to 45°C) because of the shift of Bragg wavelength in this range temperature still on wavelength VCSEL coverage. In this experiment, the performance of

temperature sensing measurement by our system is almost the same comparing to measurement by using a broadband light source and OSA and theory as well. In the last section, we checked the measurement stability for 23 hours. The result shows that the errors less than 1°C. However, practically the FBG interrogator for SHMS will be used for many years.

Chapter 8: Strain measurement

8.1 Principle of strain measurement based on a cantilever beam

We also demonstrate that our system to measure a strain by using multi-point FBG. We apply strain only FBG3, contrary the other FBGs are kept at unstrain condition. Now, we are going to introduce strain measurement based on a cantilever method. This method is very popular in the mechanic's system, especially for bridges structures. To do this, we glued FBG3 on the top surface of the cantilever beam near the fixed end as illustrated in figure 54. We employed an aluminum plate with dimensions 400 mm-long (l), 20 mm-wide (w), and 3 mm-thick (t). Many kinds of load are applied at the free end of the cantilever beam so that the FBG3 is strained following these explanations. When an aluminum with Young's modulus (E) is applied loading with force (F), the beam will deflect downward following the direction of the force. The correlation between stress (σ) and strain (ϵ) as shown in the following:

$$\epsilon = \frac{\sigma}{E} \quad 62$$

where in the beam, the stress is defined by the equation:

$$\sigma = \frac{M_c}{I} \quad 63$$

M_c is a bending moment on a cross-section where FBG3 is placed. The bending moment can be calculated by using:

$$M_c = \frac{FL.t}{2} \quad 64$$

Where L is a distance from FBG3 to free end where a force loaded. I is moment inertia of the beam. Due to, in our experiment using a plate, the moment inertia is defined by equation 65:

$$I = \frac{wt^3}{12} \quad 65$$

So equation 64 and equation 65 substitute into equation 63, we obtain:

$$\sigma = \frac{6FL}{wt^2} \quad 66$$

And finally, equation 66 substitute to equation 62, we can obtain strain on the cross-section where FBG is placed [33], [76]–[81] in equation 67. In our experiment, we used to load from a mass of battery, therefore FBG3 was obtained strain from $369 \mu\epsilon \sim 2137 \mu\epsilon$.

$$\epsilon = \frac{6FL}{wt^2 E} \quad 67$$



Figure 54. Strain measurement by using the cantilever beam method.

8.2 Strain FBG identification by scanning wavelength

Next, we observe our system to measure strain with the following condition: FBG1 and FBG2 are unstrained, whereas FBG3 is strained at $722 \mu\epsilon$ as illustrated in figure 55. The measured result is shown in figure 56. The horizontal axis represents the distance in km, and the vertical represents the magnitude of the beat signal in a.u. Unlike figure 50 in Chapter 7, which is found all the beat signals of FBGS when unstrained and room temperature, in figure 56 we find two peaks corresponding to beat signals from FBG1 and FBG2 when the wavelength was tuned to 1560.703 nm as shown in figure 56(a), there is no beat signal from FBG3. Due to FBG1 and FBG2 are unstrained in this experiment, the wavelength of 1560.703 nm corresponds approximately to the Bragg wavelength of unstrained FBG. Conversely, when the wavelength was tuned to 1561.187 nm , we only find the beat signal of FGB3, as shown in figure 56(b), which corresponds to the Bragg wavelength of FBG strained approximately $722 \mu\epsilon$.

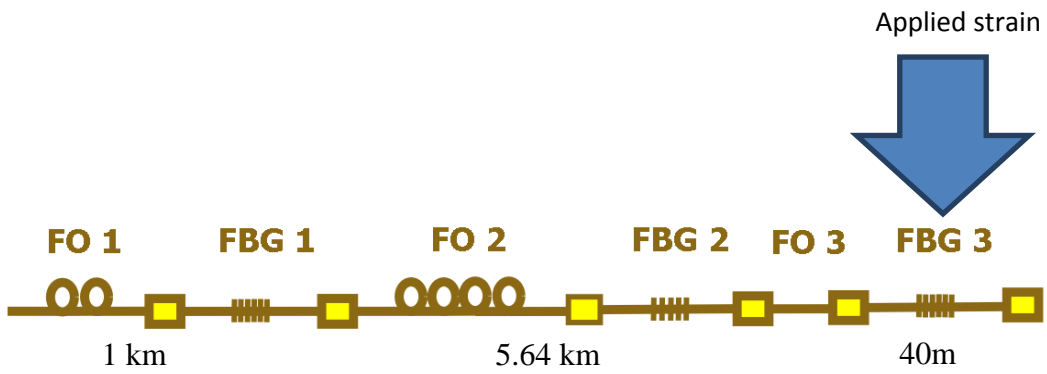


Figure 55. Illustration of measurement strain measurement using the proposed system.

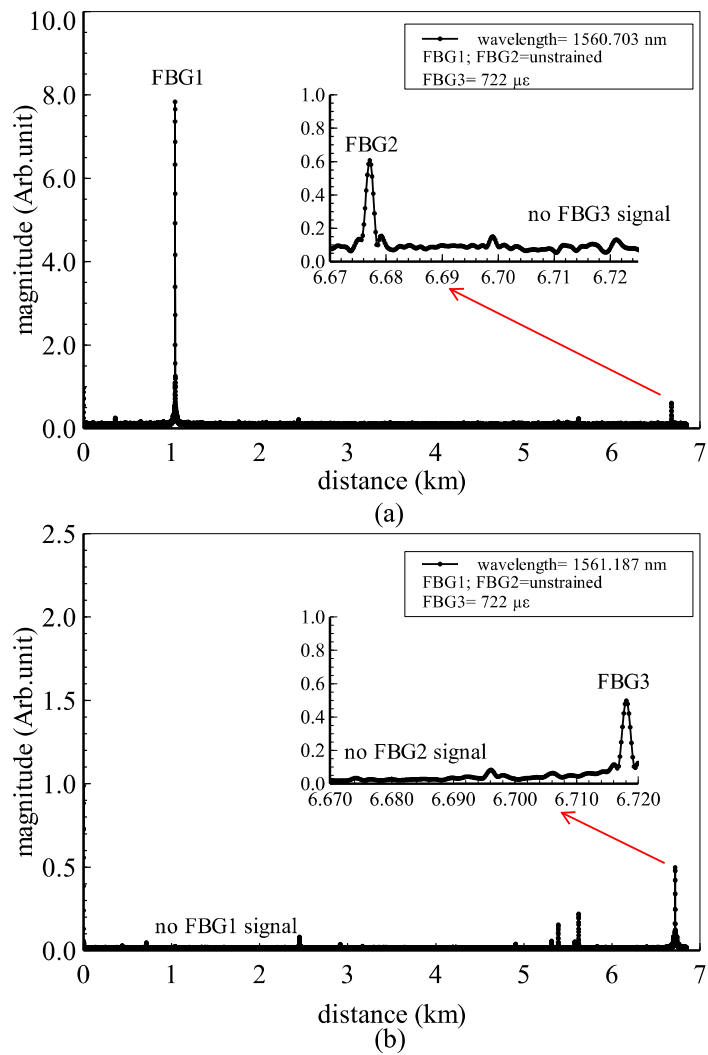


Figure 56. Measured beat spectrum for wavelength of (a) 1560.703 nm, (b) 1560.187 nm. FBG1 and FBG2 are unstrained, and FBG3 is strained at 722 $\mu\epsilon$.

8.3 Spectrum profile when FBG strain change

Like temperature measurement, we also demonstrate the spectrum profile of FBGs as a function of the strain change. FBG1 and FBG2 are still in unstrained condition, and FBG3 is strained in the range of $369 \mu\epsilon \sim 1076 \mu\epsilon$. The measured beat spectra are shown in figure 57(a), (b) and (c) for FBG1, FBG2, and FBG3, respectively. The horizontal axis is Bragg wavelength in nm, and the vertical axis is the magnitude of the spectrum in A.u. In figure 57(c), the Bragg wavelength of FBG3 is shifted to longer wavelengths with the strain. However, the Bragg wavelength of FBG1 and FBG2 are almost unchanged because FBG1 and FBG2 were unstrained as shown in figure 57(a) and (b).

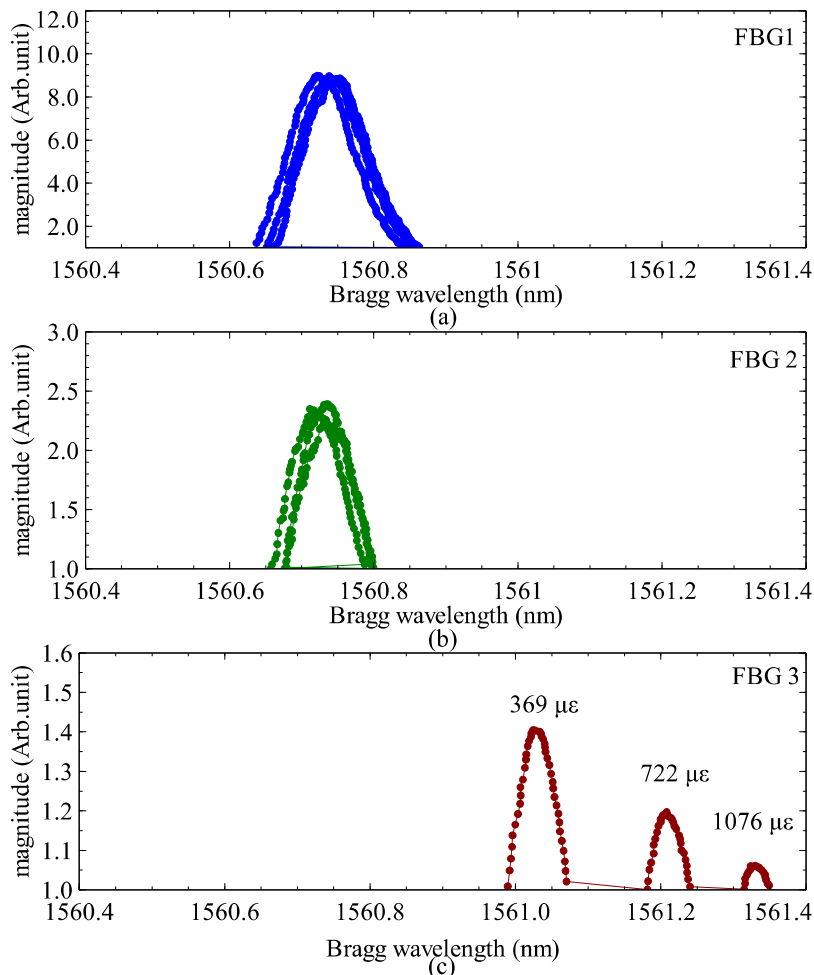


Figure 57. Spectrum of (a) FBG1, (b) FBG2, and (c) FBG3 when FBG3 is strained and FBG1 and FBG2 are unstrained.

8.4 Transfer function of strain FBG sensor

Figure 58 shows the correlation between the strain and the Bragg wavelength of the FBG3. The horizontal axis is a strain in microstrain, and the vertical axis is Bragg wavelength in nm. Similar to the correlation between Bragg wavelength and temperature, the Bragg wavelength is also linearly changed with the strain, as expressed in equation 14. From this figure, we also define the strain sensitivity is $0.29 \text{ pm}/\mu\epsilon$, which is lower than a typical FBG strain sensitivity of $1.2 \text{ pm}/\mu\epsilon$ [32], [35], [36], [39]. The relatively low sensitivity may be due to not optimized fixing of the FBG to the cantilever beam. We also compare to strain measurement results by OSA and ASE as a broadband light source. The result is also shown in figure 58. The blue line is a result measurement by using OSA and ASE, and the red line is a result measurement by using VCSEL or FBG interrogator which developed by the proposed method. Both results show almost the same trends and correlations.

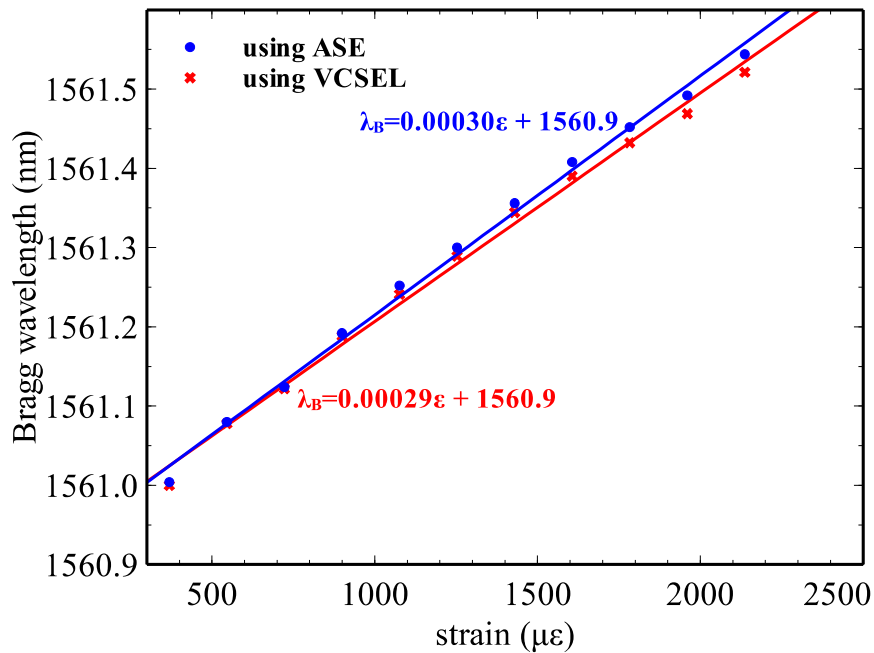


Figure 58. Transfer function of strain FBG sensor.

8.5 Cross-sensitivity and decreased magnitude issue

As we know from theory and experiment results, FBG is sensitive to both strain and temperature, so cross-sensitivity in FBG between them is a problem.

Other researchers have been reported several methods to overcome the problem, such as a combination of FBG and Fabry-Perot interferometer, superstructure method [37], FBG reference [80], and coating with a polymer material [40]. These methods are easily applied to our system.

In our proposed system, we encountered the FBGs which are installed at a far distance; the magnitude of the spectrum decreased because the Bragg wavelength of all the FBGs is almost same, and then the number of FBGs may be limited. However, this problem can be overcome by the optimization of the optical power of the VCSEL and the reflectivity and the bandwidth of FBGs.

8.6 Summary

Before we conducted the experiment for strain measurement by using our system, we briefly introduce strain measurement based on the cantilever beam method. As we have presented and discussed in this chapter, besides capable of measuring temperature, our system has been successful in performing measuring strain as well. The strain of three FBGs can be recognized by Bragg wavelength and location. The Bragg wavelength shift in this experiment corresponds to strain change on the aluminum plate that measured by FBG3. Like temperature measurement, we also compare to the result of measurement by using a broadband light source with OSA and theory as well. The result of using our system and OSA are almost same.

Chapter 9: Conclusion

9.1 Summary

We have developed and tested a system to interrogate multipoint FBG sensors combined by the I-FMCW optical ranging system and a VCSEL. Our proposed system has been successfully to measure long-range distance, temperature sensing, and strain sensing. Our system has tested to measure temperature from 25°C to 45°C and strain from 369 μm to 2137 μm . We offer a low-cost for multiplexing FBGs sensor interrogator as comparing with other techniques because our system uses commercially available VCSEL as a wavelength-tunable laser source. Our system also has great potential for remote SHMS because of the system capable of identifying the location of sensors from the beat frequency, and the physical parameters such as temperature and strain from the Bragg wavelength. Even though in our experiment, the system tested for monitoring temperature and strain, the developed system is able to be improved to measure various physical parameters such as stress, crack, and load in the monitored structure.

We also have presented the stability of our FBG interrogator for 23 hours as a temperature sensing measurement in our laboratory. Due to the FBG interrogator will be applied to monitor structures for a long time, it should be tested more a long time (for months and years). A field study of the proposed system is also needed to validate the effectiveness of detecting physical parameter change caused by damage of structures.

9.2 Future Works

In order to apply in real SHMS application, we have to increase the number of FBGs in our proposed system. Although we have demonstrated three FBGs in the range of 6.6 km, it would be possible to involve many FBGs in large-scale or long-range SHMS. In our experiments, we used FBGs with about 5% reflectivity, and the possible number of FBG can be installed only 20 FBGs. As reported in reference [3], 17 FBGs were used for the SHMS of a 500 m-long bridge. The number of FBG sensors need more than 100 if we want to monitor a

bridge over 1 km-long. We then plan to propose a method to increase the number of FBGs up to 100 by using FBGs with low reflectivity for instance 1%. The other method to increase the number of FBG sensors again can be carried out by spatial multiplexing of FBG sensor array. The laser light from a VCSEL is switched between the FBG sensor arrays by using a multi-channel optical switch. For instance, if the number of FBGs for each FBG sensor array is 50 and two FBG sensor arrays are spatial multiplexed using a multi-channel optical switch, a possible number to be installed 100 FBGs sensors. However, it needs further study on the effect of the number of FBGs in the long-range by using the I-FMCW optical ranging system.

In the experiment, we have also demonstrated strain measurement by using a cantilever beam. However, in the real application SHMS, for example, in the bridge, the system should be capable of measure a dynamic strain because every time the strain on bridge will be changed. Therefore, a further study of dynamic strain needs to improve our system, for example increasing the speed of wavelength-swept on VCSEL.

REFERENCE

- [1] R. M. Measures, *Structural Monitoring with Fiber Optic Technology*. 2001.
- [2] P. Ferdinand, “The Evolution of Optical Fiber Sensors Technologies During the 35 Last Years and Their Applications in Structure Health Monitoring,” in *7th European Workshop on Structural Health Monitoring*, 2014, pp. 914–929.
- [3] M. Nishio, “Quality Evaluation of Fiber-Optic Strain Data Acquired in Long-Term Bridge Monitoring,” *Sensors Mater.*, vol. 29, no. 2, pp. 141–152, 2017.
- [4] J. M. López-higuera, L. R. Cobo, A. Q. Incera, and A. Cobo, “Fiber Optic Sensors in Structural Health Monitoring,” *J. Light. Technol.*, vol. 29, no. 4, pp. 587–608, 2011.
- [5] F. Ansari, “Structural health monitoring with fiber optic sensors,” *Front. Mech. Eng. China*, vol. 4, no. 2, pp. 103–110, 2009.
- [6] K. Srimannarayana, M. S. Shankar, R. L. N. S. Prasad, T. K. K. Mohan, S. Ramakrishna, G. Srikanth, and S. R. P. Rao, “Fiber Bragg grating and long period grating sensor for simultaneous measurement and discrimination of strain and temperature effects,” *Opt. Appl.*, vol. 38, no. 3, pp. 601–608, 2008.
- [7] R. Rajinikumar, M. Suesser, K. G. Narayankhedkar, G. Krieg, and M. D. Atrey, “Fiber Bragg Grating Sensors for Measuring Temperature and Strain Simultaneously at Cryogenic Temperature,” in *AIP Conference Proceedings*, 2008, vol. 985, pp. 383–390.
- [8] H. Murayama, D. Wada, and H. Igawa, “Photonic Sensors Structural Health Monitoring by Using Fiber-Optic Distributed Strain Sensors With High Spatial Resolution,” *Photonic Sensors*, vol. 3, no. 4, pp. 355–376, 2013.
- [9] J. Kim, C. Kim, S. Choi, and B. Y. Lee, “Enhanced Strain Measurement Range of an FBG Sensor Embedded in Seven-Wire Steel Strands,” *Sensors*, vol. 17, pp. 1–11, 2017.
- [10] R. Di Sante, “Fibre Optic Sensors for Structural Health Monitoring of

- Aircraft Composite Structures: Recent Advances and Applications,” *Sensors*, vol. 15, pp. 18666–18713, 2015.
- [11] B. Das and V. Chandra, “Fiber-MZI-based FBG sensor interrogation : comparative study with a CCD spectrometer,” *Appl. Opt.*, vol. 55, no. 29, pp. 8287–8292, 2016.
- [12] J. Chen, B. Liu, and H. Zhang, “Review of fiber Bragg grating sensor technology,” *Front. Eptoelectron. China*, vol. 4, no. 2, pp. 204–212, 2011.
- [13] S. Yamashita, Y. Nakazaki, R. Konishi, and O. Kusakari, “Wide and Fast Wavelength-Swept Fiber Laser Based on Dispersion Tuning for Dynamic Sensing,” *J. sensors*, vol. 2009, no. June, pp. 1–12, 2009.
- [14] Q. Liu, Y. Wang, Z. Li, P. Shen, Y. Hou, H. Wang, and L. Liang, “High-speed interrogation system of multi-encoding weak FBGs based on FDML wavelength swept laser,” *Opt. Laser Technol.*, vol. 107, pp. 54–58, 2018.
- [15] T. Hariyama, P. A. . Sandborn, M. Watanabe, and M. C. Wu, “High-accuracy range-sensing system based on FMCW using low-cost VCSEL,” *Opt. Express*, vol. 26, no. 7, pp. 1496–1503, 2018.
- [16] C. Belmonte, L. Frasunkiewicz, T. Czyszanowski, H. Thienpont, J. Beeckman, K. Neyts, and K. Panajotov, “Optimization of electrically tunable VCSEL with intracavity nematic liquid crystal,” *Opt. Express*, vol. 23, no. 12, pp. 15706–15715, 2015.
- [17] H.-S. Lee, H. D. Lee, H. J. Kim, J. Du Cho, M. Y. Jeong, and C. Kim, “A Fiber Bragg Grating Sensor Interrogation System Based on a Linearly Wavelength-Swept Thermo-Optic laser Chip,” *Sensors*, vol. 14, pp. 16109–16116, 2014.
- [18] A. Caliman, A. Sirbu, A. Mereuta, K. Pier, V. Iakovlev, and E. Kapon, “14XX nm-wavelength electrically-pumped VECSELs fabricated by wafer fusion,” *Opt. Express*, vol. 21, no. 11, pp. 424–426, 2013.
- [19] A. Lytkine, W. Jager, and J. Tulip, “Frequency tuning of long-wavelength VCSELs,” *Spectrochim. Acta Part A*, vol. 63, pp. 940–946, 2006.
- [20] P. Qiao, K. T. Cook, K. Li, and C. J. Chang-hasnain, “Wavelength-Swept VCSELs,” *IEEE J. Sel. Top. Quantum Electron.*, vol. 23, no. 6, p. 1700516, 2017.

- [21] S. Moon and E. S. Choi, "VCSEL-based swept source for low-cost optical coherence tomography," *Biomed. Opt. Express*, vol. 8, no. 2, pp. 19712–19723, 2017.
- [22] R. K. Ula, Y. Noguchi, and K. Iiyama, "Three-Dimensional Object Profiling Using Highly Accurate FMCW Optical Ranging System," *J. Light. Technol.*, vol. 37, no. 15, pp. 3826–3833, 2019.
- [23] W. Hofmann, "InP-based long-wavelength VCSELs and VCSEL arrays for high-speed optical communication," Technische Universität München, 2009.
- [24] W. Stewart, B. Van Hoe, G. Van Steenberge, S. Schultz, and K. Peters, "Spectral profile tracking of multiplexed fiber Bragg grating sensors," *Opt. Commun.*, vol. 357, no. December, pp. 113–119, 2015.
- [25] Z. Luo, H. Wen, and H. Guo, "An Interrogation System Based on Two Semiconductor Optical Amplifiers for Weak Fiber Bragg Gratings," *Photonics Sensors*, vol. 4, no. 2, pp. 168–172, 2014.
- [26] G. Xin, L. Zhengying, W. Fan, W. Yiming, W. Changjia, Z. Siyue, and Y. Haihu, "Distributed sensing technology of high-spatial resolution based on dense ultra-short FBG array with large multiplexing capacity," *Opt. Express*, vol. 25, no. 23, pp. 28112–28122, 2017.
- [27] A. Barrias, J. R. Casas, and S. Villalba, "A Review of Distributed Optical Fiber Sensors for Civil Engineering Applications," *Sensors*, vol. 16, no. 748, pp. 1–35, 2016.
- [28] K. Yuksel, M. Wuilpart, V. Moeyaert, and P. Mégret, "Optical Frequency Domain Reflectometry : A Review," in *ICTON*, 2009, pp. 3–7.
- [29] C. Baker, Y. Lu, J. Song, and X. Bao, "Incoherent optical frequency domain reflectometry based on a Kerr phase-interrogator," *Opt. Express*, vol. 22, no. 13, pp. 15370–15375, 2014.
- [30] S. Liehr, "Fibre Optic Sensing Techniques Based on Incoherent Optical Frequency Domain Reflectometry," *Elektrotechnik und Informatik der Technischen Universität Berlin*, 2015.
- [31] S. J. Mihailov, "Fiber Bragg Grating Sensors for Harsh Environments," *Sensors*, vol. 12, pp. 1898–1918, 2012.

- [32] M. M. Werneck, R. C. S. B. Allil, B. A. Ribeiro, and F. V. B. De Nazaré, “A Guide to Fiber Bragg Grating Sensors,” in *Current Trends in Short- and Long-period Fiber Gratings*, 2013, pp. 1–24.
- [33] A. Setiono, R. K. Ula, D. Hanto, and B. Widiyatmoko, “laser diode low frequency vibrations measurement Prototype Fiber Bragg Gratings (FBG) Sensor Based on Intensity Modulation of the Laser Diode Low Frequency Vibrations Measurement,” in *International Symposium on Frontier of Applied Physics (ISFAP)*, 2016, vol. 30003, pp. 1–6.
- [34] P. Puranto, D. Hanto, A. Setiono, R. K. Ula, and B. Widiyatmoko, “Analysis of fiber Bragg grating responsivity in the cantilever system using ANOVA,” in *Conference on Fundamental and Applied Science for Advanced Technology (ConFAST 2016)*, 2016, pp. 1–6.
- [35] C. E. Campanella, A. Cuccovillo, C. Campanella, A. Yurt, and V. M. N. Passaro, “Fibre Bragg Grating Based Strain Sensors: Review of Technology and Applications,” *Sensors*, vol. 18, pp. 1–27, 2018.
- [36] T. Eftimov, “Sensor applications of fiber bragg and long period gratings,” in *Optical Waveguides Sensing and Imaging*, 2008, pp. 1–23.
- [37] J. Skaar, “Synthesis and characterization of fiber Bragg gratings,” The Norwegian University of Science and Technology, 2000.
- [38] V. R. Pachava, S. Kamineni, S. S. Madhuvarasu, K. Putha, and V. R. Mamidi, “FBG Based High Sensitive Pressure Sensor and Its Low-Cost Interrogation System With Enhanced Resolution,” *Photonic Sensors*, vol. 5, no. 4, pp. 321–329, 2015.
- [39] M. Ramakhrisnan, G. Rajan, Y. Semenova, and G. Farrell, “Overview of Fiber Optic Sensor Technologies for Strain / Temperature Sensing Applications in Composite Material,” *Sensors*, vol. 16, no. 99, pp. 1–27, 2016.
- [40] P. Lu, L. Men, and Q. Chen, “Resolving cross sensitivity of fiber Bragg gratings with different polymeric coatings,” *Appl. Phys. Lett.*, vol. 92, no. 171112, pp. 1–3, 2008.
- [41] Tokyo Measuring Instruments Labs., “FBG Fiber-optic Sensing System,” 2019. [Online]. Available:

https://tml.jp/e/knowledge/special_ins/fiber_measurement.html. [Accessed: 23-Nov-2019].

- [42] B. Varghese P, D. Kumar R, M. Raju, and K. N. Madhusoodanan, "Photonic Sensors Implementation of Interrogation Systems for Fiber Bragg Grating Sensors," *Photonic Sensors*, vol. 3, no. 3, pp. 283–288, 2013.
- [43] J. Zhang, G. D. Peng, L. Yuan, W. Sun, and W. Jin, "Simultaneous long- and short-gauge strain measurement in spectral domain by a novel optical fiber sensor unit," *IEEE Photonics Technol. Lett.*, vol. 19, no. 14, pp. 1084–1086, 2007.
- [44] H. Zhu, B. Shi, and C. Zhang, "FBG-Based Monitoring of Geohazards : Current Status and Trends," *Sensors*, vol. 17, pp. 1–23, 2017.
- [45] T. C. Buck, M. S. Muller, and A. W. Koch, "Theoretical Assessment of an All-Optical Temporal Low-Pass Filter for Dynamic Fiber Bragg Grating Signals," *J. Sensors*, vol. 2011, pp. 1–6, 2011.
- [46] S. F. H. Zaidi, "Advanced Dynamic Interrogation Techniques for Hybrid Distributed / Discrete Optical Fiber," Sant' Anna School, 2013.
- [47] A. D. Kersey, M. A. Davis, H. J. Patrick, M. Leblanc, K. P. Koo, C. G. Askins, M. A. Putnam, and E. J. Friebele, "Fiber Grating Sensors," *J. Light. Technol.*, vol. 15, no. 8, pp. 1442–1463, 1997.
- [48] Y. Tanaka and H. Miyasawa, "Multipoint Fiber Bragg Grating Sensing Using Two-Photon Absorption Process in Silicon Avalanche Photodiode," *J. Light. Technol.*, vol. 36, no. 4, pp. 1032–1038, 2018.
- [49] J. Sancho, S. Chin, D. Barrera, S. Sales, and L. Thévenaz, "Time-frequency analysis of long fiber Bragg gratings with low reflectivity," *Opt. Express*, vol. 21, no. 6, pp. 7171–7179, 2013.
- [50] R. S. Quimby, *Photonics and Lasers : An Introduction*, First Edit. John Wiley & Sons, New Jersey, 2006.
- [51] M. Badar, "Long Range Measurement and High Spatial Resolution Optical Frequency Domain Reflectometry Based on DSB-SC Modulation," Kochi University of Technology, 2016.
- [52] S. Werzinger, A. Koehler, R. Engelbrecht, and B. Schmauss, "Spatially Resolved Fiber Bragg Grating Sensing Using Wavelength Scanning

- Incoherent OFDR,” in *2016 Optical Fiber Communications Conference and Exhibition (OFC)*, 2016, pp. 6–8.
- [53] D. Tosi, “Review and Analysis of Peak Tracking techniques for Fiber Bragg Grating Sensors,” *Sensors*, vol. 17, no. 2368, pp. 1–35, 2017.
- [54] W. Zhang, M. Zhang, X. Wang, Y. Zao, B. Jin, and W. Dai, “The Analysis of FBG Central Wavelength Variation with Crack Propagation Based on a Self-Adaptive Multi-Peak Detection Algorithm,” *Sensors*, vol. 19, pp. 1–26, 2019.
- [55] D. Tosi, M. Olivero, and G. Perrone, “Performance analysis of peak tracking techniques for fiber Bragg grating interrogation systems,” *J. Microwaves, Optoelectron. Electromagn. Appl.*, vol. 11, no. 2, pp. 252–262, 2012.
- [56] M. Azadeh, *Fiber Optics Engineering*, First. New York: Springer, 2009.
- [57] G. P. Agrawal, *Fiber-Optic Communications Systems*, 3rd ed., vol. 6. New York: A John Wiley Interscience & Sons Inc, 2002.
- [58] A. Karim, S. Björilin, J. Piprek, and J. E. Bowers, “Long-Wavelength Vertical-Cavity Lasers and Amplifiers,” *IEEE J. Sel. Top. Quantum Electron.*, vol. 6, no. 6, pp. 1244–1253, 2000.
- [59] R. Stevens, “Modulation Properties of Vertical Cavity Light Emitters,” Royal Institute of Technology, 2001.
- [60] M. A. A.-A. Syed and M. K. Hassan, “Design of a LW-VCSEL Optical Source,” *Int. J. Adv. Res. Electr. Instrum. Eng.*, vol. 3, no. 12, pp. 13451–13460, 2014.
- [61] R. L. Roberto, “Vertical-Cavity Surface-Emitting Lasers: Advanced Modulation Formats and Coherent Detection,” Technical University of Denmark, 2013.
- [62] R. Michalzik and K. J. Ebeling, “Operating Principles of VCSELs,” in *Vertical-Cavity Surface-Emitting Laser Devices*, 2004, pp. 53–98.
- [63] C. J. Chang-Hasnain, “Tunable VCSEL,” *IEEE J. Sel. Top. Quantum Electron.*, vol. 6, no. 6, pp. 978–987, 2000.
- [64] J. Zheng, *Optical Frequency-Modulated Continuous-Wave (FMCW) Interferometry*, First. New York: Springer, 2005.

- [65] G. Breed, "A Tutorial Introduction to Optical Modulation Techniques," *High Frequency Electronics*, no. May, pp. 1–2, May-2007.
- [66] T. D. Germann, W. Hofmann, A. M. Nadtochiy, J. Schulze, A. Mutig, A. Strittmatter, and D. Bimberg, "Electro-optical resonance modulation of vertical-cavity surface-emitting lasers," *Opt. Express*, vol. 20, no. 4, pp. 5099–5107, 2012.
- [67] N. A. M. Lazam, "A Novel Technique of Optical Frequency Sweep Linearization of DFB Laser for High Resolution FMCW Reflectometry," Kanazawa University, 2016.
- [68] A. Vasilyev, "The Optoelectronic Swept-Frequency Laser and Its Applications in Ranging , Three-Dimensional Imaging , and Coherent Beam Combining of Chirped-Seed Amplifiers," California Institute of Technology, 2013.
- [69] J. Zheng, "Signal Analysis of Optical Frequency-Modulated Continuous-Wave Interference," in *Frontiers in Optics 2007*, 2007, vol. 372, no. 1960, p. 4198.
- [70] J. Zheng, "Analysis of optical frequency modulated continuous-wave interference," *Appl. Opt.*, vol. 43, no. 21, pp. 4189–4198, 2004.
- [71] K. Iiyama, S. Matsui, T. Kobayashi, and T. Maruyama, "High-Resolution FMCW Reflectometry Using a Single-Mode Vertical-Cavity Surface-Emitting Laser," *IEEE Photonics Technol. Lett.*, vol. 23, no. 11, pp. 703–705, 2011.
- [72] C. Rauscher, V. Janssen, and R. Minihold, *Fundamentals of Spectrum Analysis*, 6th ed. Munchen: Rohde & Schwarz GmbH & Co.KG, 2008.
- [73] S. Kurt, "Range resolution improvement of FMCW Radars," Midle East Technical University, 2007.
- [74] M. Enckell, B. Glisic, F. Myrvoll, and B. Bergstrand, "Evaluation of a large-scale bridge strain , temperature and crack monitoring with distributed fibre optic sensors," *J. Civ. Struct Heal. Monit*, vol. 1, no. March, pp. 37–46, 2011.
- [75] J. Song, W. Li, P. Lu, Y. Xu, L. Chen, and X. Bao, "Long-Range High Spatial Resolution Distributed Temperature and Strain Sensing Based on

- Optical Frequency-Domain Reflectometry,” *IEEE Photonics J.*, vol. 6, no. 3, pp. 1–8, 2014.
- [76] H. T. Wang, B. Zhao, Y. Dai, and G. Huang, “Fiber Bragg Grating Sensor for Strain Sensing in Low Temperature Superconducting Magnet,” *IEEE Trans. Appl. Supercond.*, vol. 20, no. 3, pp. 1798–1801, 2010.
- [77] R. Lima, R. Tavares, S. O. Silva, P. Abreu, M. T. Restivo, and O. Frazão, “Fiber Bragg grating sensor based on cantilever structure embedded in polymer 3D printed material,” in *25th International Conference on Optical Fiber Sensors*, 2017, pp. 7–10.
- [78] X. Song, Y. Zhang, and D. Liang, “Load Identification for a Cantilever Beam Based on Fiber Bragg Grating Sensors,” *Sensors*, vol. 17, no. 1733, pp. 1–21, 2017.
- [79] Q. Chen, X. Zhang, Y. Chen, and X. Zhang, “A method of strain measurement based on fiber Bragg grating sensors,” *Vibroengineering PROCEDIA*, vol. 5, no. sep, pp. 140–144, 2015.
- [80] M. Maheshwari, S. Chuan, Y. Yang, and A. Asundi, “Wavelength-shifted chirped FBGs for temperature compensated strain measurement,” *Sensors Actuators A. Phys.*, vol. 265, no. October, pp. 231–235, 2017.
- [81] P. Kelly, *Mechanics Lecture Notes: An introduction to Solid Mechanics*. 2019.

Publication

Part of this dissertation thesis is also published in an article with a title:

Low-Cost Interrogation of Long-Distance and Multipoint FBG Sensor Using Incoherent-FMCW Optical Ranging System, Dwi Hanto and Koichi Iiyama, IEEE Sensors Journal, Vol – Issue – No -, pp. , 2020.